RNA Selectively Modulates Activity of Virulent Amyloid PSMα3 and Host Defense LL-37 via Phase Separation and Aggregation Dynamics

Bader Rayan[1], Eilon Barnea[1], Rinat Indig[1], Christian F. Pantoja[2], Jesse Gayk[3], Yael Lupu-Haber[4], Alexander Upcher[5], Amir Argoetti[1], Jacob Aunstrup Larsen[6], Alexander K. Buell[6], Markus Zweckstetter[2,7], and Meytal Landau[1,3,8,9*]

[1] Department of Biology, Technion-Israel Institute of Technology, Haifa 3200003, Israel

[2] German Center for Neurodegenerative Diseases (DZNE), 37075 Göttingen, Germany

[3] CSSB Centre for Structural Systems Biology, Deutsches Elektronen-Synchrotron DESY, 22607 Hamburg, Germany

[4] The Life Sciences and Engineering Infrastructure Center, Technion-Israel Institute of Technology, Haifa 3200003, Israel

[5] Ilse Katz Institute for Nanoscale Science and Technology, Ben Gurion University of the Negev, Beer-Sheva, Israel

[6] Department of Biotechnology and Biomedicine, Technical University of Denmark DTU, 2800 Kongens Lyngby, Denmark

[7] Department for NMR-based Structural Biology, Max Planck Institute for Multidisciplinary Sciences, 37077 Göttingen, Germany

[8] The Center for Experimental Medicine, Universitätsklinikum Hamburg-Eppendorf (UKE), Hamburg, Germany

[9] European Molecular Biology Laboratory (EMBL), Hamburg, Germany

* Correspondence to meytal.landau@desy.de

Abstract

Amyloids, classically linked to neurodegenerative diseases, also play critical roles in infection and immunity. Phenol-soluble modulins (PSMs) from *Staphylococcus aureus* are virulent amyloids that contribute to cytotoxicity, immune modulation, and biofilm stability. PSMα3 forms cross-α amyloid fibrils and shares sequence and structural features with LL-37, a human host-defense peptide that assembles into α-helical structures. Here, we uncover RNA as a potent, context-dependent modulator of their aggregation and activity. RNA consistently reduces LL-37's cytotoxicity toward human cells without compromising its antibacterial function, suggesting a selective host-protective mechanism. In contrast, RNA preserves PSMα3's cytotoxic and antimicrobial activity over time, likely by promoting liquid–liquid phase separation (LLPS) and stabilizing bioactive fibrillar polymorphs, enabling *S. aureus* to fine-tune its virulence strategies. At higher concentrations, RNA drives both peptides toward distinct aggregated states, amorphous for LL-37 and fibrillar for PSMα3, underlying their divergent functional outcomes. The amyloid inhibitor EGCG abolishes the bioactivity of both PSMα3 and LL-37, overriding RNA's modulatory effects. Together, our findings establish RNA as a key modulator of both virulent amyloids and host-defense peptides, with broad implications for microbial immune evasion, innate immunity, and amyloid-associated diseases. Moreover, they highlight phase transitions as a tunable mechanism for regulating peptide bioactivity and a promising therapeutic target across infectious and neurodegenerative conditions.

Introduction

Bacterial amyloids are proteins capable of forming ordered fibrils, playing a crucial role in biofilm stability, surface adherence, cell toxicity and immune responses[1–8]. These amyloids are vital for the survival and virulence of many bacteria, enabling them to colonize and persist in diverse environments[9–11]. Some examples of bacterial amyloids include the Csg and Fap proteins from *Enterobacteria* and *Pseudomonas* species[2,7,9,12], respectively, which play a role in biofilm stability. The phenol-soluble modulins (PSMs) produced by *Staphylococci* contain amyloid-forming short peptides which play multiple functional roles central to the pathogenicity and immune evasion strategies of *S. aureus*[13–21] .

Among bacterial amyloids, PSMα3 stands out as highly cytotoxic against a broad range of microbial and human cell types[22,23]. It adopts a unique cross-α amyloid structure, where α-helices are stacked perpendicular to the fibril axis in paired sheets[22–24]. The formation of cross-α amyloids has been correlated with toxic activity, and the properties of these fibrils may regulate PSMα3's various functions[3,25,26]. PSMα3 shares self-assembly of α-helices with LL-37, a human host defense peptide[27]. Moreover, the LL-37 antimicrobial active core (residues 17–29) shows sequence similarity to PSMα3, and the formation of fibrils composed of densely packed cationic amphipathic α-helices[28]. The similarity supported the hypothesis that PSMα3 might recapitulate functions of LL-37, and indeed, they share the activation of the signal inhibitory receptor on leukocytes-1 (SIRL-1) which is a negative regulator of myeloid cell function and dampens antimicrobial responses[29]. Such common functions might be related to molecular mimicry and the ability of bacterial peptides to hijack immunomodulation pathways[30]. Indeed, PSMαs interact with the formyl peptide receptor 2 (FPR2) on immune cells, initiating immune responses such as chemotaxis, phagocytosis, and the secretion of pro-inflammatory cytokines. These reactions are critical for recruiting and activating immune cells, thereby amplifying the inflammatory response[15,31–36].

LL-37 has been shown to bind RNA released from dying cells, forming stable complexes that protect the RNA from enzymatic degradation and promote its uptake by dendritic cells[37]. Once

internalized, these RNA–LL-37 complexes activate Toll-like receptors (TLRs), triggering cytokine production and dendritic cell maturation[37]. Beyond LL-37, other human antimicrobial peptides (AMPs), such as β-defensins, also form higher-order assemblies that organize nucleic acids into nanostructures with defined periodicity. These nanocomplexes potently stimulate TLRs, highlighting that innate immune activation is influenced not only by ligand identity, but also by the nanoscale geometry and spatial organization of the complexes[38–40].

Interestingly, nucleic acid interactions also play a key role in the immune activation triggered by bacterial amyloids. For example, PSMs co-assemble with extracellular DNA (eDNA), and CpG-rich DNA specifically promotes PSMα3 fibrillation, forming co-aggregates that colocalize with DNA in biofilms. These complexes activate TLR pathways and induce anti-dsDNA autoantibody responses in mice[41]. Similar mechanisms are seen in *E. coli* and *Salmonella*, where curli fibers bind eDNA, enhance fibrillation, and engage TLRs signaling, also promoting autoimmunity[42,43]. These findings suggest that amyloid–DNA complexes in bacterial biofilms are not only structural components but also potent immunomodulators with potential links to autoimmunity.

The similarities between LL-37 and PSMα3 prompted us to investigate their interaction with RNA and the resulting structural and functional implications on cell toxicity. Our findings show that both PSMα3 and LL-37 can undergo liquid-liquid phase separation (LLPS) in the presence of RNA, and transition into solid aggregates as a function of incubation time and RNA concentration. LLPS is in general a critical process in cellular organization in which proteins or other molecules separate into distinct liquid phases, forming dynamic, membraneless compartments central to cellular processes such as metabolism, RNA regulation, and stress response[44–47]. PSMα3 also penetrates HeLa cells, localizes within the nucleolus, and colocalizes with nucleic acids. We observed dynamic and reversible molecular behavior within the nucleolus, mirroring in vitro observations of PSMα3's LLPS with RNA.

Epigallocatechin gallate (EGCG), a polyphenol primarily found in green tea and recognized as an amyloid inhibitor[4,48–50], disrupts the cytotoxicity and antibacterial activity of both PSMα3 and

LL-37. In contrast, RNA differentially modulates their activity, suggesting distinct mechanisms linked to their self-assembly dynamics, morphologies, and toxic pathways. These findings provide new insights into RNA-mediated self-assembly in bacterial physiology and highlight potential biomedical applications for combating resistant *S. aureus* infections.

Results

PSMα3 interacts with RNA in vitro

The interactions between PSMα3 and RNA were assessed using an Electrophoretic Mobility Shift Assay (EMSA), comparing the binding affinity of PSMα3 to single-stranded PolyA RNA and double-stranded Poly (AU) RNA. The RNA molecules were labeled with the IR800CW fluorescent dye (as detailed in the Methods section). Freshly dissolved PSMα3, at varying concentrations, was incubated with each RNA type at a constant concentration for 30 minutes at 37°C. The EMSA results revealed that PSMα3 exhibits a stronger binding affinity to double-stranded Poly (AU) RNA, as evidenced by significant shifts at lower peptide concentrations compared to single-stranded Poly(A) (Fig. 1A).

A high density of PSMα3 fibrils was observed after 2 hours of incubation with Poly (AU) RNA using transmission electron microscopy (TEM), while incubation with Poly(A) RNA under the same conditions resulted in amorphous aggregation (Fig. 1B). Consequently, we decided to focus our subsequent investigations on the behavior of PSMα3 in the presence of double-stranded Poly (AU) RNA.

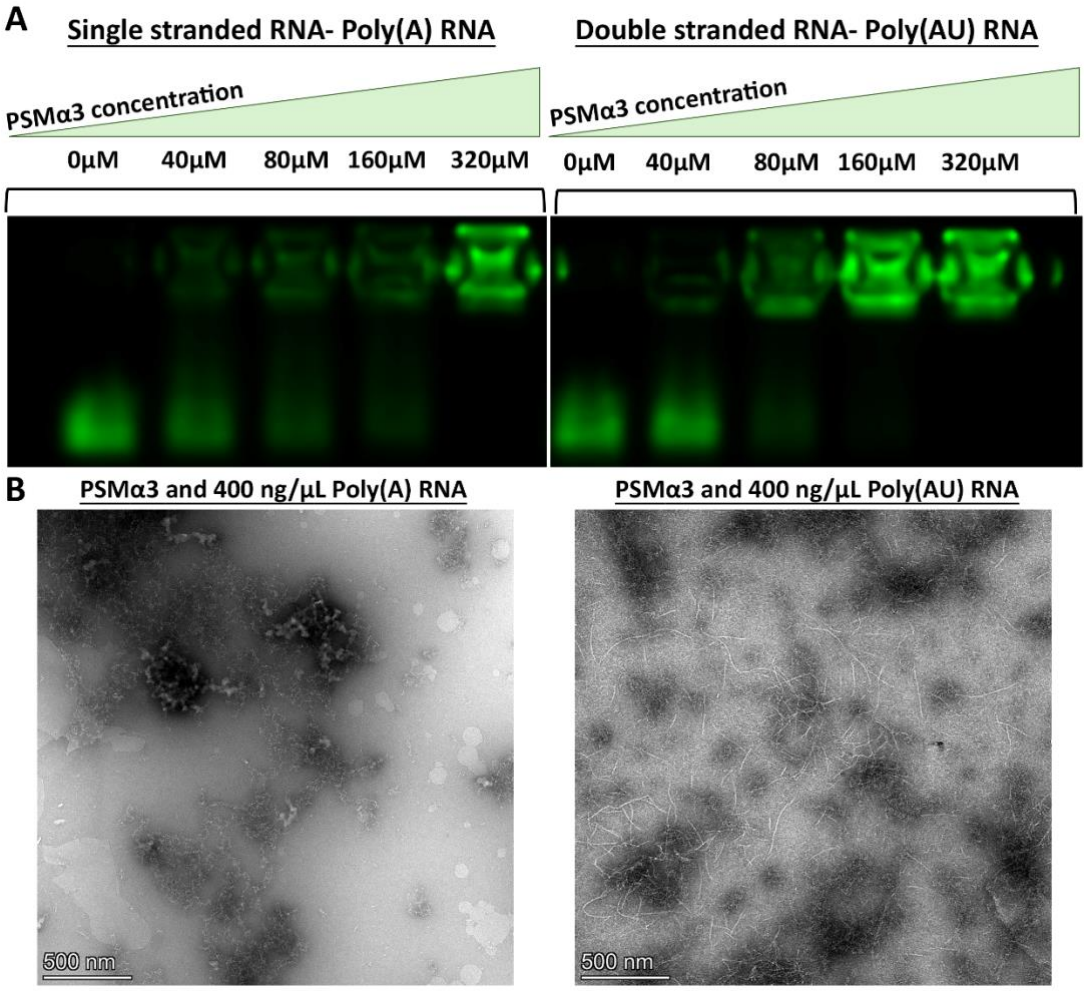

Figure 1. The binding and effect of single- and double-stranded RNA on PSMα3. (A) EMSA assay illustrating the interaction between PSMα3 and RNA. The assay compares the effects of increasing concentrations of PSMα3 (0 μM, 40 μM, 80 μM, 160 μM, and 320 μM), shown in a gradient from left to right, on the mobility shift of single-stranded Poly(A) RNA (left panel) and double-stranded Poly (AU) RNA (right panel) at ~400ng/μL. **(B)** Transmission electron micrographs of 100 μM PSMα3 incubated for 2 hours in the presence of 400 ng/μL of either Poly(A) RNA (left) or Poly (AU) RNA (right). Scale bars represent 500 nm.

Poly (AU) RNA concentration-dependent induced transitioning of PSMα3 condensates to solid aggregates

To better understand the nature of the PSMα3-RNA interaction, we visualized their mixtures via fluorescence microscopy, using PSMα3 labeled with Fluorescein isothiocyanate (FITC) at the C-terminus (PSMα3-FITC), which is known to form fibrils[22]. 100 μM PSMα3-FITC was incubated with either 50 ng/μl or 400 ng/μl propidium iodide (PI)-labeled RNA in a close to physiological buffer of 50 mM HEPES (pH 7.4) containing 150 mM sodium chloride (NaCl).

With the addition of 50 ng/μl RNA, PSMα3 formed liquid-liquid phase separated droplets that clearly colocalized with the RNA (Fig. 2A). The liquid nature of the droplets was further validated by fluorescence recovery after photobleaching (FRAP) analysis, where we observed a rapid recovery of the PSMα3-FITC signal shortly after bleaching (Fig. 2C). However, after a longer incubation of 2 hours, no fluorescence recovery was detected, suggesting that the condensates aged and transitioned to a more aggregated state (Fig. 2D). In addition, we observed the encapsulation of RNA within PSMα3-FITC “coated” droplets (Fig. S1).

In contrast to the effect of 50 ng/μl RNA, the addition of a higher RNA concentration of 400 ng/μl to PSMα3 resulted in immediate aggregation, with no observed phase of droplet formation (Fig. 2B). FRAP analysis indicated no recovery of signal after bleaching, likely due to the formation of solid structures rather than droplets with liquid-like properties (Fig. 2E). These aggregates also showed colocalization (Fig. 2B), indicating that the PSMα3-RNA interaction persisted in both the LLPS and solid states.

Turbidity assays showed that a 30 min co-incubation of 100 μM PSMα3 with varying concentrations of RNA displayed an increased turbidity up to 50 ng/μl, while higher RNA concentrations displayed a decrease in turbidity (Fig. S2). This suggests that 50 ng/μl can be a critical concentration between soluble species, which might be able to phase separate, and the formation of aggregates. The decrease in particle size above 50 ng/μL can be a result of either the formation of smaller particles or aggregation into larger clusters, which can settle out of suspension, removing them from the light-scattering medium and reducing turbidity.

Alternatively, it may indicate the dissolution of phase-separated droplets, as observed in systems like Ddx4[51]. We then used transmission electron microscopy (TEM) and total internal reflection fluorescence (TIRF) microscopy to better visualize the effect of RNA on PSMα3 morphology.

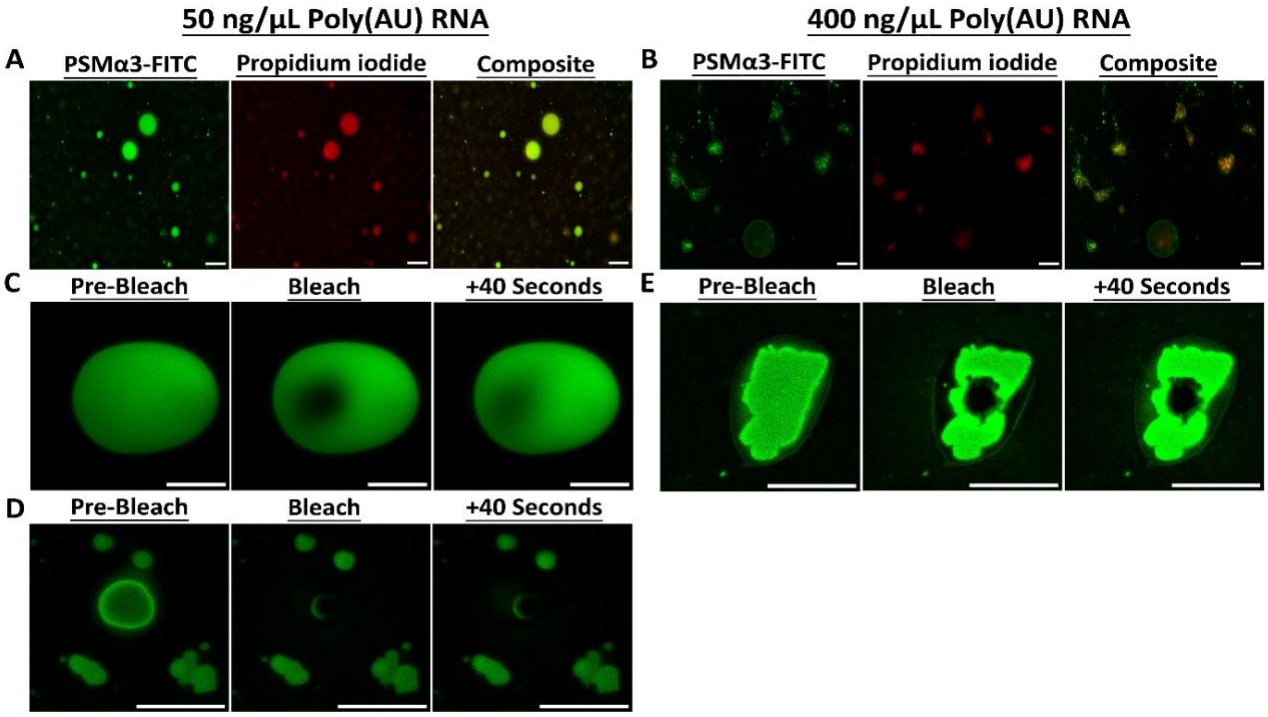

Figure 2. Colocalization, droplet formation and texture of PSMα3 mixed with varying Poly (AU) RNA concentrations. (A-B) Widefield fluorescence microscopy images of 100 µM PSMα3-FITC (green) in the presence of 50 ng/µL (**A**) or 400 ng/µL (**B**) Poly (AU) RNA (red), showing their individual and composite channel images. (**C-E**) FRAP analysis of PSMα3-FITC with 50 ng/µL Poly (AU) RNA taken after 10 min (**C**) or 2-hours co-incubation (**D**), or with 400 ng/µL Poly (AU) RNA taken after 10 min co-incubation (**E**). The images in panels C-D were captured before bleaching, immediately after bleaching, and 40 seconds post-bleaching. Scale bars in all images represent 20 µm.

RNA concentration-driven changes in PSMα3 fibrillar morphology and aggregation

The TEM micrographs showed that in the absence of RNA, 100 µM PSMα3 formed nanotube-like fibrils after 2 hours, growing wider or with some twist after 24-hours co-incubation (Fig. 3A). Incubating PSMα3 with a low concentration of 10 ng/µL RNA displayed accelerated fibril formation, with more strongly twisted, wide, sheet-like fibrils observed after both 2 hours and

24 hours (Fig. 3A). With the addition of 50 ng/μL RNA, PSMα3 fibrils have a similar twisted morphology after 2 hours, while at a longer incubation time of 24 hours, we observed a significant morphological shift into more thin amorphous aggregates (Fig. 3A). At the higher concentration of 400 ng/μL RNA, PSMα3 formed dense, thin fibrils after 2 hours, but with a possible fragmentation into smaller species or rearrangement into amorphous aggregates after 24 hours of co-incubation. This indicates that RNA concentration and time of co-incubation affect the density and morphology of PSMα3 fibrils. This corresponds to the differences observed by light microscopy of co-aggregates contexture of LLPS droplets vs solid aggregates (Fig. 2).

These observations were further supported by TIRF microscopy using the amyloid-specific dye AmyTracker630 (AT630). TIRF analysis was performed at 50 ng/μL and 400 ng/μL RNA, which induced phase separation and solid aggregation of PSMα3, respectively. With the addition of 50 ng/μL RNA to PSMα3-FITC, a strong AT630 fluorescence signal was detected after 2 hours co-incubation, but not after 30 minutes. This suggests a time-dependent transition into amyloid-like species (Fig. 3B). Conversely, at 400 ng/μL RNA, a significant AT630 fluorescence was observed already after 30 minutes of co-incubation, consistent with a rapid formation of amyloid fibrils (Fig. 3C). These findings highlight a concentration- and time-dependent modulation of PSMα3 phase separation and structural transitions, where RNA promotes LLPS at lower concentrations and drives rapid amyloid formation and unique fibrillar morphologies at higher concentrations.

Solid-state circular dichroism (ssCD) spectroscopy reveals that PSMα3 lacks a defined secondary structure both immediately after preparation and following 2 hours of incubation. However, upon addition of RNA, a clear shift toward an α-helical conformation is observed (Fig. S3). This supports the notion that RNA not only accelerates aggregation but also promotes or stabilizes the α-helical fibrillar architecture, potentially consistent with cross-α amyloid structures.

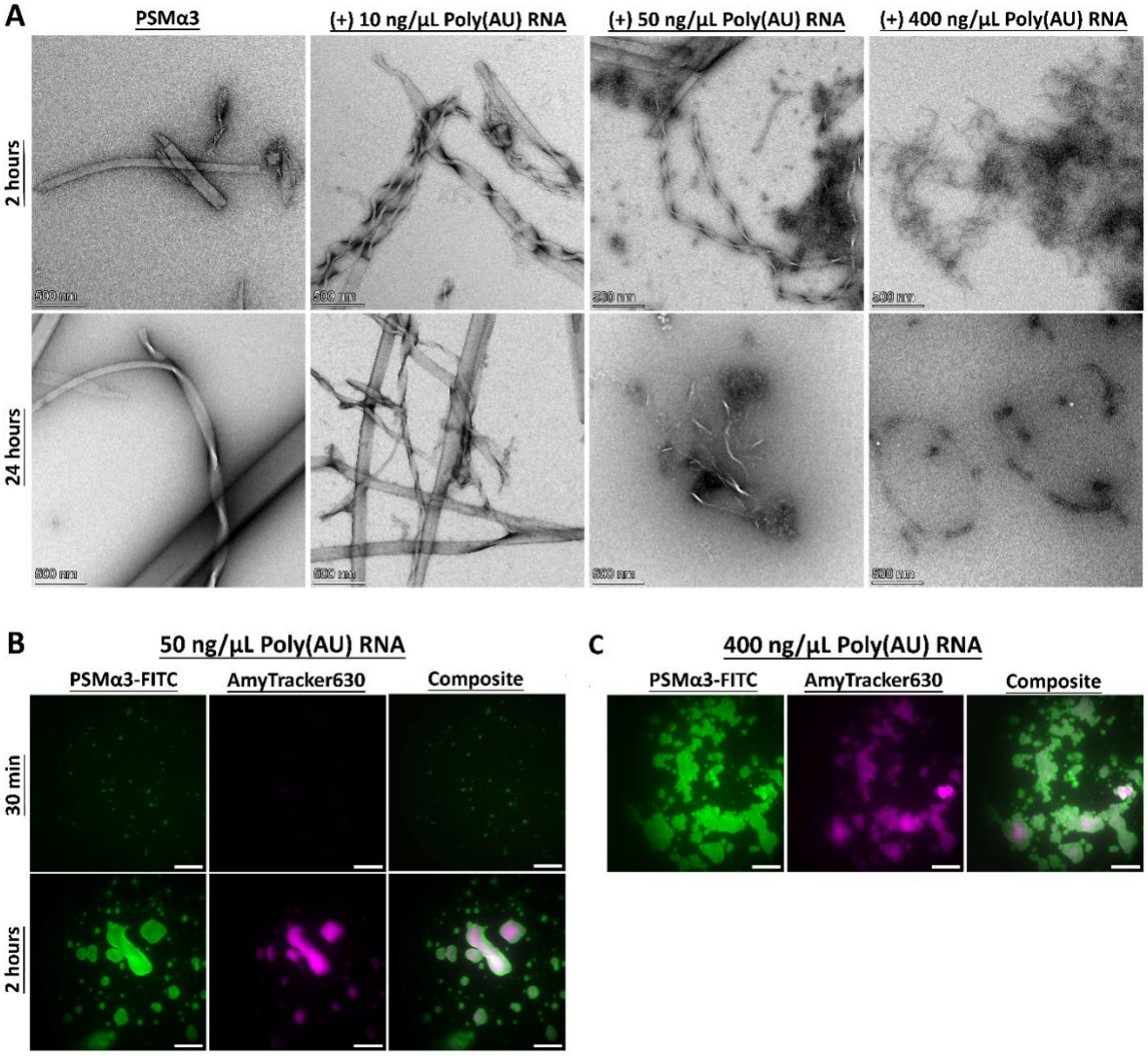

Figure 3. TEM and TIRF visualization of PSMα3 aggregation and morphology with different Poly (AU) RNA concentrations and incubation times. (A) TEM micrographs of 100 µM PSMα3 incubated with or without Poly (AU) RNA at varying concentrations of 10 ng/µL, 50 ng/µL, and 400 ng/µL for 2 hours (top row) and 24 hours (bottom row). Scale bars represent 500 nm. **(B)** TIRF microscopy images showing 100 µM FITC-PSMα3 (green) co-incubated with 50 ng/µL Poly (AU) RNA and the amyloid indicator AT630 (magenta) for 30 minutes and 2 hours. Scale bars represent 20 µm. **(C)** TIRF microscopy images of 100 µM FITC-PSMα3 (green) co-incubated with 400 ng/µL Poly (AU) RNA and AT630 (magenta) for 30 min. Scale bars represent 20 µm.

RNA modulates the antibacterial activity of PSMα3

The antimicrobial activity of PSMα3 against *Escherichia coli* was evaluated under varying RNA concentrations and incubation times using the PrestoBlue Cell Viability Assay (Fig. 4A).

Freshly dissolved 10 μM PSMα3 exhibited potent antibacterial activity, completely abolishing bacterial viability. After 2 hours of incubation, PSMα3 retained its full activity, comparable to its freshly prepared state. The presence of RNA at 50 ng/μL and 400 ng/μL had no impact on its antimicrobial function within this timeframe (Fig. 4A).

In contrast, after 24 hours of incubation, PSMα3's antibacterial activity was significantly reduced (Fig. 4A), also at 20 μM, suggesting a decrease in its effective concentration or changes in its morphology. Notably, the addition of RNA at 50 ng/μL or 400 ng/μL prevented this loss of activity, indicating that RNA plays a stabilizing role of toxic species. These findings suggest that RNA influences PSMα3 aggregation dynamics and morphology, thereby modulating its long-term antimicrobial effectiveness.

RNA modulates PSMα3 cytotoxicity against human HeLa cells

The effect of RNA on the cytotoxicity of PSMα3 against human HeLa cells was evaluated by measuring lactate dehydrogenase (LDH) release, an indicator of cell membrane damage (Fig. 4B). Freshly dissolved PSMα3 exhibited substantial cytotoxicity, causing approximately 80% cell death at 20 μM and 50% at 10 μM. The presence of RNA did not significantly alter the toxicity of freshly dissolved PSMα3 (Fig. 4B), similar to the antibacterial activity. However, following 2 hours of incubation, PSMα3 cytotoxicity was significantly reduced, possibly due to aggregation and a loss of active peptide concentration. This reduction occurred earlier than the loss of antibacterial activity, which was only observed after 24 hours of incubation (Fig. 4A). This discrepancy may reflect differences in how membrane composition and media conditions influence PSMα3 aggregation kinetics, or it may indicate distinct mechanisms underlying cytotoxicity versus antibacterial membrane disruption.

Notably, co-incubation with RNA helped maintain PSMα3 cytotoxicity in a concentration-dependent manner. With 50 ng/μL RNA, the 2-hour incubated PSMα3 retained cytotoxicity comparable to its freshly dissolved form, suggesting that RNA prevents activity loss due to incubation. However, after 24 hours, 50 ng/μL RNA was insufficient to preserve cytotoxicity.

In contrast, at 400 ng/µL RNA, partial cytotoxicity was maintained for both 2-hour and 24-hour incubated PSMα3, compared to the freshly dissolved sample.

Overall, these findings suggest that RNA prevents the incubation-induced loss of both antibacterial activity and cytotoxicity (Fig. 4). This effect appears to be concentration- and co-incubation time-dependent, likely linked to RNA-induced morphological variations of PSMα3 species (Figs. 2&3).

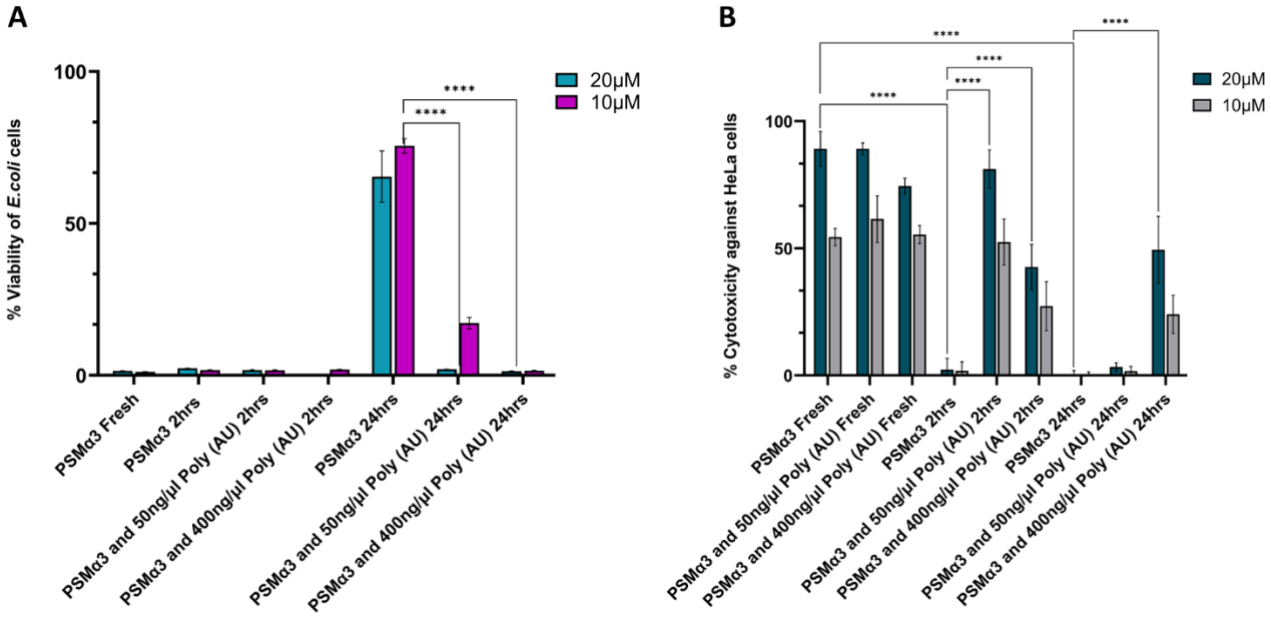

Figure 4. Impact of Poly (AU) RNA on PSMα3 cytotoxicity and antibacterial activity. Antimicrobial activity of PSMα3 against *E. Coli* using the PrestoBlue cell viability assay (**A**) and its cytotoxicity against HeLa cells using the LDH colorimetric assay (**B**) were assessed with and without Poly (AU) RNA at varying concentrations. The experiments were performed in at least three replicates and repeated across three independent days to ensure result reliability. Cytotoxicity and bacterial cell viability percentages were calculated as the mean of all replicates, with error bars representing the standard error of the mean (SEM). Statistical significance was determined using one-way ANOVA for normally distributed data in GraphPad Prism (version 11). Significance levels are indicated as follows: *p<0.05, **p<0.01, ***p<0.001, ****p<0.0001.

PSMα3 targets nucleolar nucleic acids in HeLa cells with LLPS dynamics

The interactions and localization of PSMα3 were next explored in HeLa cells with the addition of 20μM FITC-PSMα3 just before imaging. PI was added to the cell medium as a marker for cell death, as it selectively penetrates dead cells and binds to their nucleic acids.

Confocal microscopy images revealed that PSMα3 induces significant toxicity as indicated by membrane damage, intracellular PSMα3 aggregate formation, and positive PI staining. PSMα3 also enters the nuclei, with a notable concentration in the nucleolus, indicated by the foci of green fluorescence (marked by white arrows in Fig. 5). The composite images demonstrated clear colocalization of PSMα3 with nucleic acids in the nucleolus, as seen by the overlap of the green PSMα3-FITC signal and the red fluorescence from PI-stained nucleic acids.

FRAP analysis of 20 μM PSMα3-FITC within the nucleolus of HeLa cells indicated mobility (Fig. 5B). The Pre-bleach panel shows the initial fluorescence distribution, with the nucleolus marked by the white arrow. Following photobleaching, a localized reduction in fluorescence was observed. Notably, within 60 seconds, significant fluorescence recovery was observed in the nucleolus, highlighting the dynamic and reversible molecular behavior of PSMα3 in this cellular compartment. The results overall suggest an interaction between PSMα3 and nucleolar RNA/DNA within cells, which mirrors our in vitro findings where PSMα3 interacted, and underwent LLPS and formed solid aggregates in the presence of RNA.

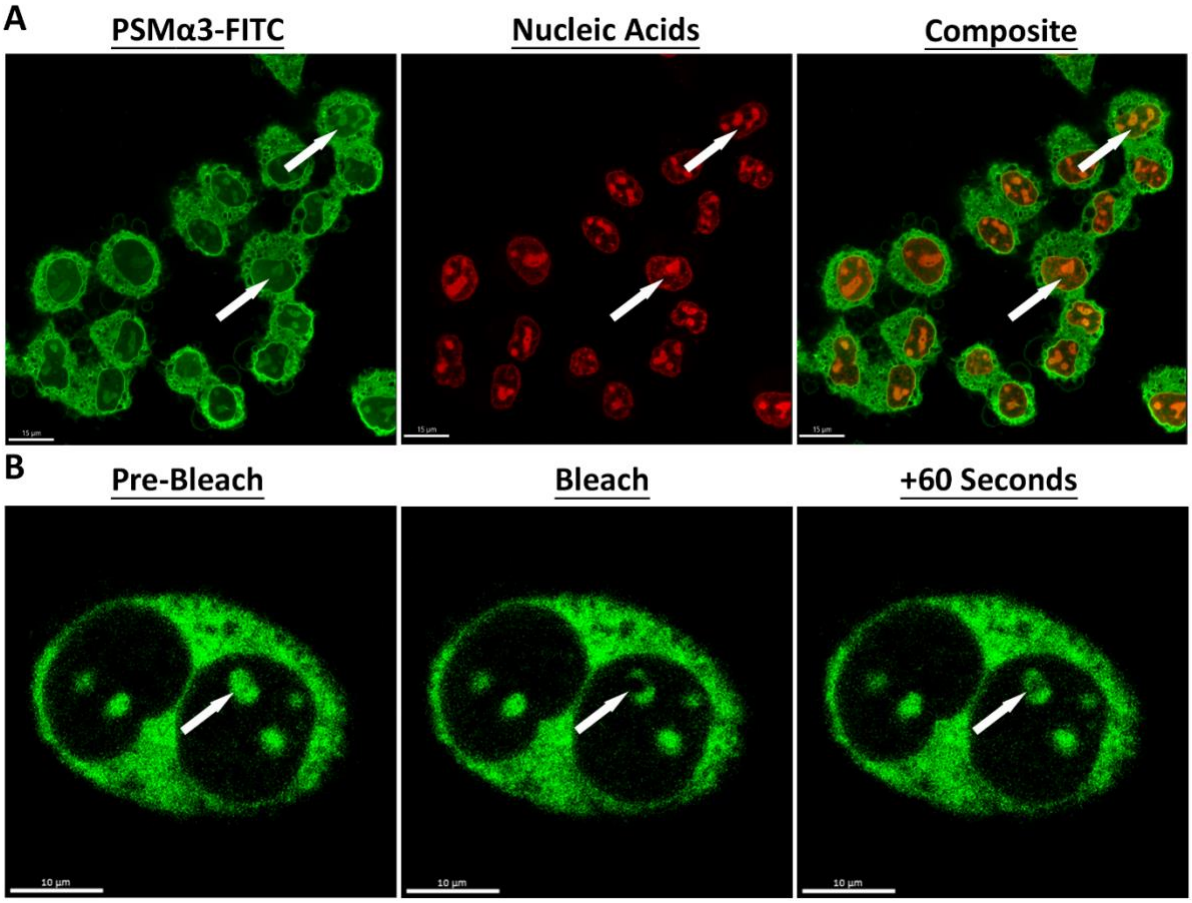

Figure 5. Colocalization of PSMα3 with nucleic acids in HeLa cells. (A) Confocal microscopy images showing the localization and colocalization of 20 μM PSMα3-FITC (green) and nucleic acids stained with PI (red) inside the nucleolus of HeLa cells (indicated in arrows). The left panel illustrates the distribution of PSMα3 within the cell. The middle panel shows the nucleic acids stained with PI. The right panel is a composite image that demonstrates the colocalization of PSMα3 with nucleic acids. Scale bars represent 15 μm. **(B)** FRAP analysis of 20 μM FITC-labeled PSMα3 inside the nucleolus (indicated by the arrow) of HeLa cells, showing fluorescence recovery after 60 seconds. Scale bars represent 10 μm.

EGCG directly binds PSMα3 and inhibits its fibrillation and bioactivity, even in the presence of RNA

Since RNA appears to protect or maintain PSMα3's toxic functions, potentially by influencing its fibril formation and morphology, we investigated the corresponding and combined effects

of an inhibitor of fibril formation. One such inhibitor is epigallocatechin gallate (EGCG), the most abundant catechin in tea and a known amyloid inhibitor, including of PSMs[4].

The addition of EGCG to PSMα3 at a 1:1 molar ratio did not significantly alter its cytotoxicity against HeLa cells. However, at a fivefold molar excess, EGCG completely abolished PSMα3's cytotoxic effect (Fig. 6C). To examine the structural changes underlying this effect, we analyzed fibril formation kinetics and morphology in the presence of EGCG. TEM micrographs revealed that a fivefold molar excess of EGCG disrupted fibril formation of 100 μM PSMα3, instead inducing amorphous aggregates (Fig. 6A). Consistently, kinetics assays of fibril formation showed that EGCG inhibited the Thioflavin-T (ThT) fluorescence curve otherwise indicating the fibril formation of 100 μM PSMα3 (Fig. S4). These findings suggest that EGCG reduces PSMα3 toxicity by modulating its fibril formation and morphology. The addition of RNA did not counteract the effect of EGCG or restore PSMα3 cytotoxicity (Fig. 6C), highlighting the strong impact of EGCG on PSMα3 morphology and properties.

To investigate residue-specific interactions between PSMα3 and EGCG, we performed NMR spectroscopy using a 2:1 PSMα3:EGCG molar ratio. The 1D ^{1}H-NMR spectrum revealed distinct chemical shift changes and peak broadening upon EGCG addition, particularly in residues Glu8/Met1 and Glu2, suggesting specific interactions between these sites and the EGCG molecule (Fig. 7A). Peak broadening was also observed in the aromatic region of EGCG, especially for protons H1 and H2, compared to the reference spectrum of EGCG alone, indicating that the interaction is visible from the EGCG side as well. Notably, slight opalescence was observed in the sample following preparation, potentially reflecting early-stage aggregate formation. Additionally, the presence of multiple cross-peaks between non-sequential residues (i+3 or i+4) in the two-dimensional (2D) ^{1}H-^{1}H Nuclear Overhauser Effect Spectroscopy (NOESY) spectrum indicates a well-defined structure of PSMα3 in this condition (Fig. 7B). The 2D ^{1}H-^{1}H Total Correlation Spectroscopy (TOCSY) spectrum displayed connectivity between backbone amide (HN) and alpha protons (Hα) for several assigned

residues, while the 2D ^{1}H-^{1}H NOESY spectrum revealed spatial correlations between nearby residues (i+1).

To assess the temporal stability of the sample, we monitored signal intensities over a 3-day period. PSMα3 signals remained stable, with only a ~10% decrease in intensity, whereas EGCG signals exhibited substantial degradation, with nearly 50% loss over the same time frame (Fig. 7C). Given the ~1.5-day duration of the 2D NMR measurements, it is estimated that over 60% of EGCG remained in solution during data acquisition, allowing for reliable observation of its interaction with the peptide. Of note, EGCG's activity has been shown to depend on its chemical stability and the surrounding conditions. Specifically, at neutral pH, EGCG may undergo oxidation, and its inhibitory effects could be attributed to its degradation products rather than the intact compound itself[52].

Live-cell confocal microscopy provided further insights into how EGCG binding affect PSMα3 interactions with cells. A fivefold molar excess of EGCG prevented the toxic effects of 20 μM PSMα3, blocking cell penetration and PI staining (Fig. 6B, top panel). Instead, PSMα3-FITC formed extracellular aggregates and showed no interaction with cell membranes, as indicated by the absence of PI staining and intact cell membranes (Fig. 6B, bottom panel).

Furthermore, EGCG at a fivefold molar excess also reduced the antibacterial activity of PSMα3 against *E. coli*, maintaining bacterial cell viability (Fig. S5). Super-resolution fluorescence microscopy showed that while 20 μM PSMα3 typically aggregates on the bacterial membrane, causing membrane disruption and PI staining indicative of cell death (Fig. S5), EGCG at a

fivefold molar excess prevented membrane aggregation and PI staining, thereby preserving membrane integrity.

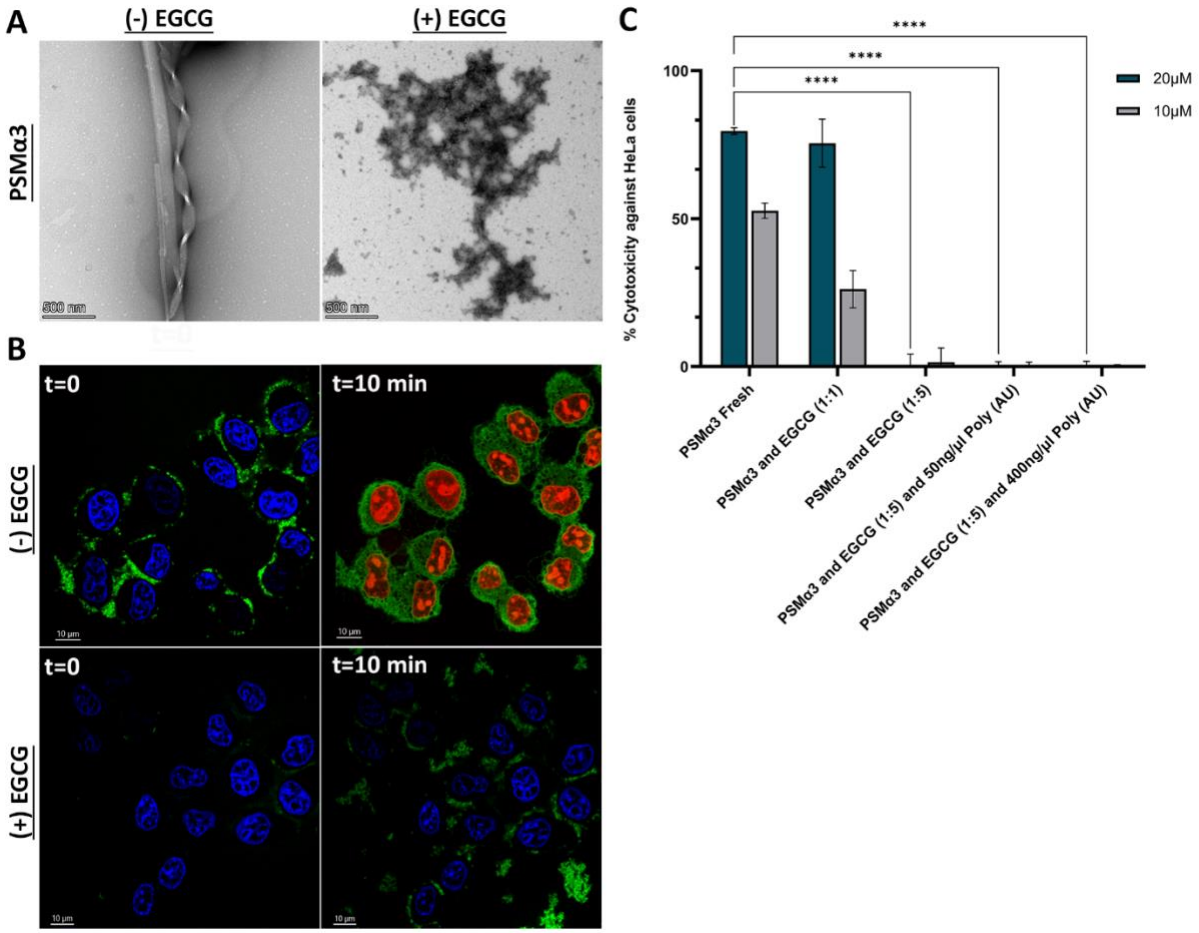

Figure 6. EGCG modulates PSMα3 aggregation and reduces toxicity against HeLa cells. (**A**) TEM micrographs of 100 µM PSMα3 incubated for 24 hours, without (left) and with (right) a fivefold molar excess of EGCG. Scale bars: 500 nm. (**B**) Live-cell confocal microscopy of HeLa cells treated with 20 µM PSMα3-FITC (green) without (top) and with EGCG (bottom), imaged immediately after preparation (t = 0) and after 10 minutes. Hoechst 33342 (blue) marks the nuclei, while PI staining (red) indicates membrane disruption. Scale bars: 10 µm. (**C**) Cytotoxicity of PSMα3 against HeLa cells in the presence and absence of EGCG and Poly (AU) RNA at two different concentrations, assessed via LDH assay. The experiment was performed in triplicate and repeated on three separate days for consistency. Cytotoxicity percentages were averaged across all replicates, with error bars representing the standard error of the mean. Statistical significance: *$p < 0.05$, **$p < 0.01$, ***$p < 0.001$, ****$p < 0.0001$ (one-way ANOVA, GraphPad Prism v11).

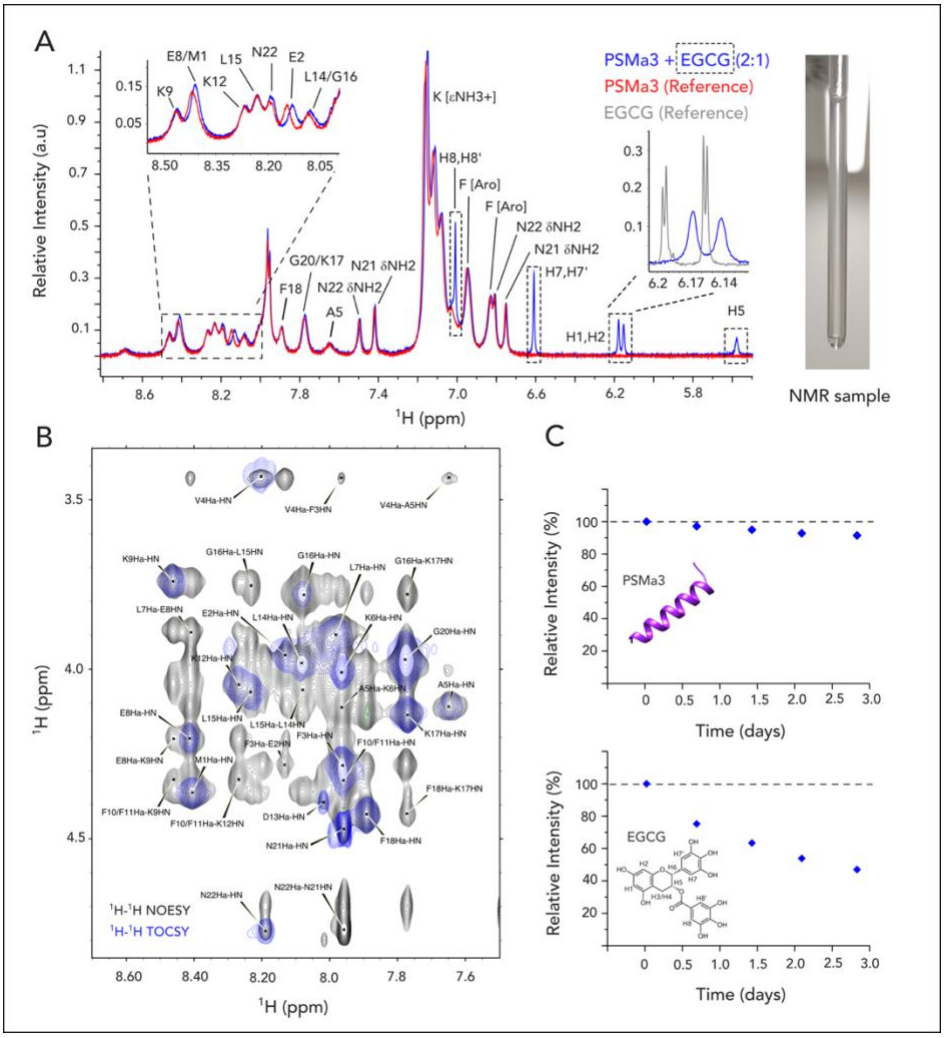

Figure 7. Residue-specific interactions between PSMα3 and EGCG. (**A**) One-dimensional (1D) ^{1}H NMR spectra of 1.0 mM PSMα3 alone (red) and in complex with 0.5 mM EGCG (blue), recorded at 35 °C. Specific residues, including Glu8/Met1 and Glu2, show chemical shift changes suggestive of direct interaction with EGCG (highlighted in the upper left). Dashed boxes mark proton signals corresponding to EGCG. Peak broadening of H1/H2 protons, compared to the EGCG-only reference sample (light gray), indicates interaction from the EGCG side. Slight opalescence observed in the sample suggests potential aggregate formation. (**B**) Two-dimensional (2D) ^{1}H–^{1}H TOCSY and NOESY spectra of the PSMα3:EGCG complex at a 2:1 ratio, recorded at 35 °C. The cross-peaks in the TOCSY spectrum allow the identification of the spin system and direct connections through the scalar coupling between the proton amide (HN) and the alpha protons (Hα) of the same residue. The cross-peaks in the NOESY spectrum establish a sequential connection between neighboring residues (i+1), allowing spectral assignment. The remaining cross-peaks (i+3 or i+4) in the spectrum support PSMα3 secondary structure in the experimental conditions. (**C**) Temporal stability of the PSMα3:EGCG sample over 3 days.

RNA modulates the human host defense peptide LL-37 phase behavior and cytotoxicity without compromising antimicrobial activity

LL-37, a human host defense peptide, shares functional, sequence, and structural similarities with PSMα3, including its ability to self-assemble and interact with nucleic acids[28,37]. We therefore examined whether RNA similarly influences LL-37 activity and properties.

Fluorescence microscopy showed that 100 μM LL-37-FITC incubated with 100 ng/μL PI-labeled Poly (AU) RNA displayed formation of aggregates, but with no indication for LLPS or droplet formation (Fig. S6). Since diverse stresses trigger phase separation of RNA-binding proteins and their coalescence into stress granules[53] , we explored the effect of RNA on LL-37 under thermal stress. We applied heat shock at 65°C for 15 minutes and found that RNA significantly affected LL-37's phase behavior in a concentration-dependent manner. Specifically, with the addition of 100 ng/μL RNA, LL-37 formed condensates that colocalized with the RNA (Fig. 8A). At 200 ng/μL RNA, LL-37 still formed droplets, but aggregation began to appear, indicating a transition from a liquid-like state to a more solid-like phase (Fig. 8B). At 400 ng/μL RNA, droplets were no longer observed, and extensive aggregation occurred, with strong colocalization between LL-37 and RNA (Fig. 8C). As a comparison of stress response, PSMα3 displayed droplet formation after the heat shock of 65°C for 15 minutes only at more conducive conditions of pH 4, but not at pH 7.4 (Figs. S7-S8). The results overall suggest that for both LL-37 and PSMα3, higher RNA concentrations promote aggregation over phase separation.

Freshly dissolved LL-37 exhibited cytotoxicity against HeLa cells, which, in contrast to PSMα3, remained consistent even after incubation for up to 24 hours. Notably, RNA significantly reduced LL-37 cytotoxicity in a concentration-dependent manner, irrespective of the incubation duration (freshly dissolved, 2 hours, or 24 hours) (Fig. 8D). This contrasts with RNA's rescuing effect on the incubation time-dependent loss of PSMα3 cytotoxicity. The antimicrobial activity of LL-37 against *E. coli* also remained unchanged upon incubation. However, unlike its effect on cytotoxicity, RNA had minimal impact on antibacterial activity,

with only high concentrations of 400 ng/μL reducing LL-37 activity (Fig. 8E). Similar to PSMα3, LL-37 cytotoxicity against HeLa cells and its antimicrobial activity was attenuated by EGCG in a concentration-dependent manner (Fig. 8E).

TEM micrographs of 100 μM LL-37 revealed a variety of aggregative and fibrous structures, including thin, curli-like fibrils, although no consistent morphology was observed (Fig. S9A). RNA induced a distinct morphological change, leading to increased aggregation and the formation of mostly amorphous species, but also some thicker, ribbon-like fibrils were observed. These structures resemble those previously observed for a segment of the LL-37 active core (residues 17–29), which is similar to PSMα3 in sequence and its ability to form fibrils of densely packed amphipathic α-helices[28]. Heat shock further intensified aggregation, resulting in denser, amorphous condensates and larger fibrillar assemblies, with and without RNA (Fig. S9B). The distinct effects of RNA on the aggregation and morphologies of LL-37 and PSMα3 may underlie the observed differences in their cytotoxic and antibacterial activities.

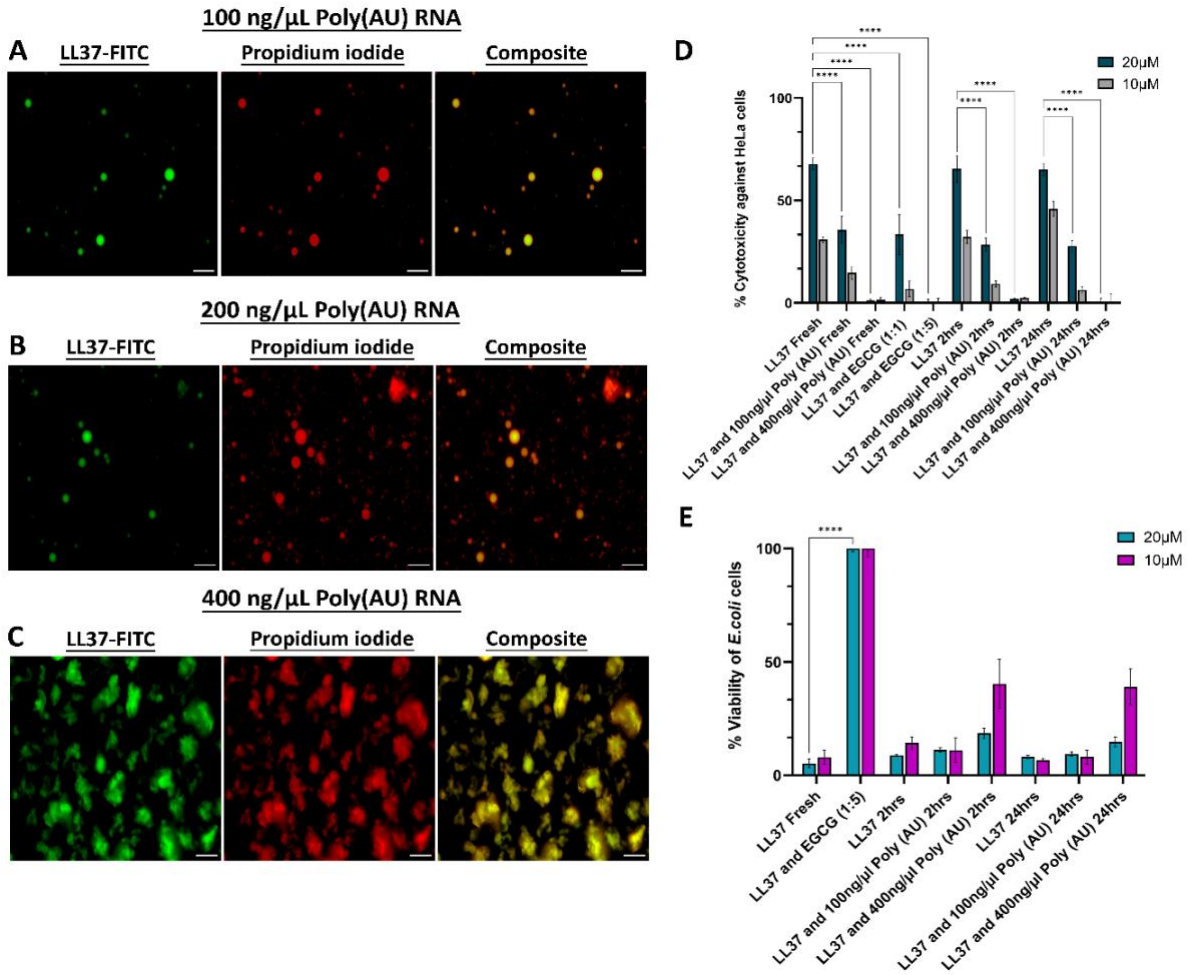

Figure 8. Effect of RNA concentration on LL37 phase separation, aggregation, and activity at pH 7 after heat shock. Fluorescence microscopy images showing LL37 (FITC-labeled, green) in the presence of increasing concentrations: 100 ng/µL (**A**), 200 ng/µL (**B**) and 400 ng/µL (**C**) of Poly (AU) RNA (PI-labeled, red) after heat shock at 65°C for 15 minutes at pH 7. Scale bars represent 20 µm. **(D)** LL37 cytotoxicity, with and without Poly (AU) RNA and EGCG at varying concentrations, was assessed in HeLa cells using the LDH colorimetric assay. The experiment was performed in triplicate and repeated on three separate days for reproducibility. Cytotoxicity percentages represent the average of all replicates, with error bars indicating the standard error of the mean. **(E)** The antimicrobial activity of LL37, with and without Poly (AU) RNA and EGCG at varying concentrations, was evaluated against *E. coli* using the PrestoBlue Cell Viability assay. The experiment was performed in triplicate and repeated on three separate days for reproducibility. Bacterial viability percentages represent the average of all replicates, with error bars indicating the standard error of the mean. Statistical significance (**D-E**): *$p < 0.05$, **$p < 0.01$, ***$p < 0.001$, ****$p < 0.0001$ (one-way ANOVA, GraphPad Prism v11).

Discussion

This study demonstrates that Poly (AU) RNA modulates the cytotoxic and antimicrobial activities of PSMα3 and LL-37 in a concentration-dependent and peptide-specific manner, revealing a regulatory mechanism that differentially influences their biological functions. The effects of RNA on these peptides are distinctly linked to their aggregation dynamics and morphological outcomes, underscoring its role as a context-specific modulator of peptide bioactivity.

Interestingly, although the supramolecular structure of LL-37 does not exhibit the characteristic amyloid cross-β or the cross-α architecture, with molecular stacking perpendicular to the fibril axis[27], it nonetheless shows functional links to amyloids. Notably, LL-37 has been reported to bind the Alzheimer's-associated amyloid-β (Aβ) peptide and inhibit its fibrillization, likely by stabilizing prefibrillar intermediates[54]. These findings suggest that LL-37 may modulate Aβ aggregation dynamics, with potential implications for aging, immune suppression, and infection[54].

Our findings demonstrate that RNA consistently reduces LL-37's cytotoxicity against human cells, independent of RNA concentration or incubation duration (Fig. 8D). Notably, this reduction in cytotoxicity does not compromise LL-37's antimicrobial activity against *E. coli* (Fig. 8E), indicating that RNA selectively protects mammalian cells while preserving its host defense functions. Unlike PSMα3, LL-37 does not undergo RNA-induced LLPS under physiological conditions, exhibiting this behavior only after thermal stress (Fig. 8). RNA rather leads to amorphous aggregates (Fig. S9), which likely underlies the selective attenuation of cytotoxicity, highlighting RNA's role in modulating LL-37's functional states.

In contrast to the results for LL-37, RNA exhibits a dynamic and concentration-dependent regulation of PSMα3's cytotoxicity and antimicrobial activity, revealing a complex interplay between phase separation and aggregation. Unlike LL-37, PSMα3 shows a time-dependent reduction in activity (Fig. 4), likely due to a transition from soluble species to irreversible fibril morphology (Fig. 3). At lower RNA concentrations, PSMα3's cytotoxic activity against human

cells is initially preserved but diminishes over time. This time-dependent decrease likely reflects a transition from soluble liquid-like droplets to solid aggregates within the RNA-PSMα3 complex. Conversely, at higher RNA concentrations, PSMα3's cytotoxicity is partially maintained even after prolonged incubation, suggesting that RNA induces a specific fibril morphology that remains reversible and bioactive.

The antimicrobial activity of PSMα3 also shows temporal modulation, with a noticeable decline after 24 hours of incubation (Fig. 4A). This delayed reduction compared to its activity against human cells suggests distinct aggregation pathways or interactions with the bacterial environment. However, RNA preserves PSMα3's antimicrobial function even after 24 hours (Fig. 4A), likely by stabilizing intermediate or alternative polymorph states, which are reversible and enable the reactivation of PSMα3.

This behavior of dynamic phase transitions and aggregation mirrors those observed in human amyloids[45,46,55–64]. For example, FUS, TDP-43, hnRNPA1, and tau rely on LLPS to perform their normal cellular functions. However, these proteins are also associated with neurodegenerative diseases like amyotrophic lateral sclerosis, frontotemporal dementia, tauopathies, and Alzheimer's disease. While LLPS enables their proper functioning under healthy conditions, mutations or modifications can disrupt this process, leading to irreversible aggregation and disease progression[55–66]. Similar to human amyloids, AMPs can also induce LLPS with nucleic acids[67]. In bacterial cells, this interaction compacts nucleic acids and disrupts critical processes like transcription and translation[67]. PSMα3 interaction with nucleic acids within human cells, particularly its localization in the nucleolus (Fig. 5), supports a comparable mechanism leading to cell death mediated by this bacterial virulence factor.

These findings reveal a sophisticated and context-specific regulation of PSMα3 and LL-37 by RNA, demonstrating that RNA can fine-tune peptide bioactivity with remarkable specificity across cell types. The specificity of RNA's effects on cytotoxicity and antimicrobial activity points to a sophisticated regulatory mechanism with significant biological implications: For PSMα3, RNA-driven LLPS and aggregation dynamics provide a flexible strategy for

modulating cytotoxicity and antimicrobial activity, enabling *S. aureus* to adapt its virulence based on environmental cues. This dynamic structural plasticity may facilitate immune evasion, biofilm formation, and enhanced survival in diverse host environments. For LL-37, RNA's selective attenuation of cytotoxicity without compromising antibacterial function suggests an evolutionary strategy to balance host defense and tissue protection. This regulatory mechanism minimizes collateral damage to host cells while maintaining effective antimicrobial activity, highlighting dual functionality in immune regulation.

These findings reveal a previously unrecognized role for RNA in regulating amyloid-like peptides, opening new avenues for RNA-targeted therapeutic interventions against bacterial infections and immune regulation. Moreover, the parallels between RNA-driven phase transitions in PSMα3 and human amyloids suggest broader implications for understanding amyloid-associated diseases. By elucidating the dual role of RNA in promoting reversible LLPS and inducing stable fibril formation, this study contributes to the growing understanding of phase behavior in functional and pathological amyloids.

Methods

Peptide and Poly (AU) RNA preparation

Unlabeled and C-terminal FITC-labeled PSMα3 and LL-37 (PSMα3-FITC and LL-37-FITC) (>98% purity) were purchased from GL Biochem (Shanghai) Ltd. Poly (AU) RNA was purchased from Sigma Aldrich. A stock solution of the peptides was prepared at a concentration of 1 mM in a mixture of 20% dimethyl sulfoxide (DMSO) and 80% ultra-pure water. For light microscopy experiments, we used a mixture of 20% FITC-labeled and 80% unlabeled PSMα3 or LL-37. The Poly (AU) RNA stock solution was prepared at a concentration of 2000 ng/μl in UPW, the stock solution was stored at −80 °C until further use. Labeled Poly (AU) RNA was prepared by introducing 0.02 mg/ml of PI dye to the Poly (AU) RNA stock solution. For the experiments, samples containing 100 μM PSMα3 or LL-37 with

Poly (AU) RNA at 10, 50, 100, 200, or 400 ng/µl were prepared in 50 mM HEPES buffer with 150 mM sodium chloride (NaCl), adjusted to pH 7.4, or in 20 µM Tris, 20 µM Bis-Tris, and 20 µM sodium acetate adjusted to pH 4.

Cytotoxicity against HeLa cells tested using the lactate dehydrogenase (LDH) release assay

Human cervical carcinoma HeLa cells (ATCC® CCL-2™) were routinely cultured in Dulbecco's Modified Eagle's Medium - high glucose (DMEM) (Sigma, Israel) with L-glutamine, and supplemented with penicillin (100 U/ml), streptomycin (0.1 mg/ml), and with 10% fetal calf serum (Sigma, Israel). The cells grown at 37°C and 5% CO2. One day before the experiment, cells were resuspended in growing medium (DMEM supplemented with 10% fetal calf serum) $1X10^5$ cells/ml. 50 µL of cell suspension were pipetted into a 96-well plate and grown over night. Thirty minutes before the experiment cells were washed and resuspended in 50 µL of DMEM medium supplemented with L-glutamine (100 U/mL), and with penicillin (100 U/mL), streptomycin (0.1 mg/mL), and with 0.5% heat-inactivated fetal calf serum (assay medium). For the cytotoxicity assay, 100 µM PSMα3 was incubated with or without EGCG at molar ratios of 1:1 or 1:5, or with Poly (AU) RNA at concentrations of 50 ng/µL or 400 ng/µL, for the designated incubation times. Similarly, 100 µM LL-37 was prepared under the same conditions, with or without EGCG at 1:1 or 1:5 molar ratios, or Poly (AU) RNA at 100 ng/µL or 400 ng/µL, following the specified incubation times.

Serial two-fold dilutions in assay medium were performed, and 50 µL of each dilution were pipetted into the three different 96-well with the cells. The plates were incubated for 30 min at 37°C and 5% CO2 and then cell lysis was quantified using the LDH release colorimetric assay according to the manufacturer’s instructions, including all recommended controls (LDH; Cytotoxicity Detection Kit Plus, Roche Applied Science, Germany). Cell-free assay medium was measured as background. Cells subjected to the same experimental conditions apart from peptide addition were used as a control to account for spontaneous LDH release. Cells subjected to the same experimental conditions apart from peptide addition and treated with

manufacturer-supplied lysis buffer were used as a control to account for maximum LDH release. Absorbance at 490 and 690 nm was measured in a plate reader (FLUOstar Omega, BMG Labtech, Germany). Absorbance at 690 nm was subtracted from 490 nm readings to correct for background. The mean absorbance of triplicate samples and controls was calculated, followed by background subtraction. Data was obtained from at least three independent biological replicates, with the arithmetic mean used for averaging. Error bars represent the standard deviation (SD). Statistical analysis, including one-way ANOVA, was performed using GraphPad Prism 10.

Assessment of Bacterial Viability Using PrestoBlue™ HS Cell Viability Reagent

Escherichia coli (E. coli) cultures were grown overnight in Luria Broth (LB) medium at 37 °C with shaking at 220 rpm. PSMα3 and LL-37 stock solutions were prepared by dissolving the peptides at a concentration of 1 mM in a solvent mixture of 20% DMSO and 80% ultra-pure water. From these stock solutions, the following sample preparations were made:

For PSMα3: **(1)**100 μM PSMα3 **(2)**100 μM PSMα3 with 50 ng/μL Poly (AU) RNA **(3)** 100 μM PSMα3 with 400 ng/μL Poly (AU) RNA **(4)** 100 μM PSMα3 with 500 μM EGCG. For LL-37: **(1)**100 μM LL-37 **(2)**100 μM LL-37 with 100 ng/μL Poly (AU) RNA **(3)** 100 μM LL-37 with 400 ng/μL Poly (AU) RNA **(4)** 100 μM LL-37 with 500 μM EGCG.

All solutions were prepared in 50 mM HEPES buffer pH 7.4 containing 150 mM NaCl. Where applicable, samples were incubated for the specified durations of 2 hours or 24 hours.

On the day of the experiment, dilutions of the PSMα3 solutions to 20 μM and 10 μM were prepared in LB medium and dispensed into a sterile 96-well black flat-bottom plate (Greiner bio-one). *E. coli* cultures were diluted to an optical density (OD) of 0.2, and bacterial suspensions were added to the wells. The plate was incubated at 37 °C with shaking at 220 rpm for 1 hour to allow the reaction to proceed.

Following incubation, 10X PrestoBlue™ HS Cell Viability Reagent (Invitrogen) was added to the wells. Wells containing only LB medium served as negative controls, while wells containing

only *E. coli* served as positive controls. Plates were sealed with a thermal seal film (EXCEL Scientific) and incubated in a plate reader (CLARIOstar). Bacterial viability was assessed using PrestoBlue fluorescence (excitation: 535–560 nm; emission: 590–615 nm) over time. Each condition was tested in triplicate across three independent experiments. Fluorescence values were averaged, and blank readings were subtracted. Antimicrobial activity was determined at the 2-hour time point, when fluorescence was highest in the positive control. Data were obtained from at least three independent biological replicates, with the arithmetic mean used for averaging. Error bars represent the standard deviation (SD). Statistical analysis, including one-way ANOVA, was performed using GraphPad Prism 10.

Transmission electron microscopy (TEM)

For TEM analysis, 4–5 µL of 100 µM PSMα3, with or without EGCG or Poly(AU) RNA at concentrations of 10 ng/µL, 50 ng/µL, and 400 ng/µL, as well as 100 µM LL-37, with or without Poly(AU) RNA at 100 ng/µL and 400 ng/µL, were directly applied onto glow-discharged 400-mesh copper grids (easiGlow; Pelco, Clovis, CA, USA) with a grid hole size of 42 µm, stabilized with Formvar/carbon (Ted Pella, Inc.). The grids were glow-discharged using a 15-mA current with a negative charge for 25 seconds. Samples were allowed to adhere to the grids for 45 seconds before being stained with a 1% uranyl acetate solution (Electron Microscopy Science, 22400-1) for 45 seconds. The samples were then examined using a ThermoFisher Scientific (FEI) Talos F200C transmission electron microscope, operating at 200 kV and equipped with a Ceta 16M CMOS camera, at the Ilse Katz Institute for Nanoscale Science and Technology, Ben Gurion University of the Negev, Israel.

Turbidity measurements

Turbidity measurements were performed using a FLUOstar Omega plate reader (BMG Labtech) set to a wavelength of 400 nm. For each sample, the protein concentration was maintained at 100 µM, while RNA concentrations were varied across the following levels: 10 ng/µl, 20 ng/µl, 50 ng/µl, 100 ng /µl, 200 ng/µl, and 400 ng/µl. The turbidity of the mixtures was monitored over several hours following resuspension. The maximum absorbance recorded

within the first 30 minutes was used as an indicator of the dense phase volume. The experiments were conducted three times with similar observations.

Electrophoretic mobility shift assay (EMSA)

RNA molecules were synthesized by IDT, with oligoA modified by the IRDye 800CW fluorescent dye. Double-stranded RNA was prepared by annealing 10 μM oligoA-IRDye 800CW with 10 μM oligoU in an annealing buffer containing 10 mM Tris-HCl (pH 7.5), 50 mM NaCl, and 1 mM EDTA. The mixture was heated to 95°C for 5 minutes, followed by gradual cooling to 25°C at a rate of 2°C per minute. The final RNA concentration used in the binding reactions was 40 nM (~400ng/μL).

RNA-protein complexes were incubated at 37°C for 30 minutes before being resolved on a 2.5% agarose gel. Gel electrophoresis was performed in a 0.5× TBE buffer for 7 minutes. The complexes were visualized using a Li-Cor Odyssey FC imaging system in the 800 nm channel with a 30-second exposure. For the EMSA, binding reactions were carried out in a buffer composed of 20 mM HEPES (pH 7.9), 50 mM KCl, 1 mM Dithiothreitol (DTT), 0.1 mM Ethylenediaminetetraacetic acid (EDTA), 5% glycerol, and 0.05% nonyl phenoxypolyethoxylethanol (NP-40). PSMα3 was added to the reactions at final concentrations of 0, 40, 80, 160, and 320 μM. The experiments were conducted three times with similar observations.

Fluorescent microscopy imaging of peptides with RNA in vitro

Prior to imaging, 100 μM PSMα3 or LL-37 (containing 20% FITC-labeled and 80% unlabeled peptide) were combined with PI-labeled Poly (AU) RNA at different concentrations in 50 mM HEPES buffer pH 7.4 containing 150 mM NaCl. Sample were also tested after 65°C heat shock for 15 minutes. In addition, the PSMα3 and RNA mixture was also tested in a different buffer containing 20 μM Tris, 20 μM Bis-Tris, and 20 μM sodium acetate at pH 4 and were subjected to heat shock at 65°C for 15 minutes.

Following preparation, with or without heat shock, a 10 μL aliquot of each sample was transferred to a μ-Slide 8 Well ibidi chamber or to a clean 24 × 60 mm No. 1.5 glass slide for imaging. Fluorescence microscopy was performed using a Leica DMI8 inverted fluorescent microscope equipped with a 63× immersion oil objective (Numerical Aperture, NA = 1.4) at the Life Sciences and Engineering (LS&E) Infrastructure Center, Technion-Israel Institute of Technology, Haifa, Israel. Data were processed and analyzed using Fiji-ImageJ software. The experiment was conducted three times with similar observations.

Fluorescence recovery after photobleaching (FRAP) measurements

FRAP experiments were conducted using a Zeiss LSM 710 laser scanning confocal microscope equipped with a 63× Plan-Apochromat oil immersion objective, NA1.4, at the Life Sciences and Engineering (LS&E) Infrastructure Center, Technion-Israel Institute of Technology, Haifa, Israel. The experiments were performed on condensates from by 100 μM PSMα3-FITC or LL-37-FITC mixed with PI-labeled Poly (AU) RNA at various concentrations as indicated in the figures. Photobleaching was performed using 405 nm and 488 nm laser lines. The experiments were conducted three times with similar observations.

For FRAP analysis inside the nucleolus of HeLa cells, PSMα3 was added to the cells at a final concentration of 20 μM containing 20% FITC-labeled and 80% unlabeled peptide. The cells were incubated with the peptide for 20 minutes before conducting the experiment. Data was processed and analyzed using ZEISS ZEN software and Fiji-ImageJ software. The experiments were conducted three times with similar observations.

Total internal reflection fluorescence (TIRF) microscopy

TIRF microscopy was performed using a ZEISS Elyra 7 Super-Resolution Microscope equipped with a 63× Apochromat alpha Plan-Apochromat Oil immersion DIC objective, NA1.46, at the Life Sciences and Engineering (LS&E) Infrastructure Center, Technion-Israel Institute of Technology, Haifa, Israel. Images were acquired using the pco.edge sCMOS cameras, and data were processed and analyzed with ZEISS ZEN software to accurately

represent the observed phenomena. The condensates and aggregates analyzed were generated using 100 μM PSMα3-FITC with either 50 ng/μL or 400 ng/μL Poly (AU) RNA. AmyTracker 630 (Ebba Biotech) was added at a 1:500 (peptide: AmyTracker) molar ratio to each sample. The experiments were conducted three times with similar observations.

Confocal microscopy visualization of PSMα3 interaction with HeLa cells

HeLa cells were pre-cultured one day before the experiment by preparing a suspension containing 350,000 cells/ml and plating 150 μl of this suspension into each well of a μ-Slide 8 well glass-bottom chamber. The cells were then incubated overnight under standard growth conditions (37°C, 5% CO2) to allow for adherence and growth. On the day of the experiment, the cells were washed three times with phosphate-buffered saline (PBS) to remove any residual media. Hoechst 33342 dye (10 mg/mL stock) was diluted 1:2000 in fresh cell media and added to the cells. The cells were incubated with Hoechst for 10 minutes at 37°C and 5% CO2. After incubation, cells were washed three times with PBS to remove Hoechst residuals. A working solution of PI was prepared by diluting a 1 mg/ml PI stock solution to a final concentration of 0.02 mg/ml in fresh cell growth media. Immediately prior to imaging, PSMα3 was added to the cells at a final concentration of 20 μM containing 20% FITC-labeled and 80% unlabeled peptide. The cells were then imaged using a Ti2-E microscope by Nikon with a CSU-W1 spinning disk confocal unit by Yokogawa, equipped with a 100X CFI SR HP Plan Apochromat Lambda S silicone immersion objective, NA1.35, at the Life Sciences and Engineering (LS&E) Infrastructure Center, Technion-Israel Institute of Technology, Haifa, Israel. Confocal movies and images were captured by Photometrics BSI sCMOS cameras to observe the interaction and localization of PSMα3 within the cells, focusing particularly on its colocalization with nucleic acids in the nucleolar region. The acquired images and movies were subsequently analyzed using Imaris Image Analysis Software (Oxford Instruments). The experiments were conducted three times with similar observations.

Super resolution light microscopy visualization of PSMα3 interaction with *E. coli*

E. coli lptD4213 cells were a kind gift from Prof. Sima Yaron from the Technion – Israel Institute of Technology. An inoculum was pre-cultured in Luria-Bertani medium (LB) medium at 220 rpm and 37°C for 24 hours prior to the experiment. On the day of the experiment, the optical density (OD) of the culture was measured, and the cells were diluted to an OD of 0.4. The cells were then incubated with 20 μM PSMα3, with and without EGCG at 1:5 molar ratio, alongside a bacteria-only control. Samples were incubated for 30 minutes at 220 rpm and 37°C. Following incubation, the samples were centrifuged three times for 3 minutes at 1.5g, with the supernatant discarded and the pellet resuspended in 1X PBS after each spin. The resuspended cells were then stained with 50 μg/mL wheat germ agglutinin (WGA) CF633 for 30 minutes. After staining, the cells were washed three times by centrifugation with PBS to remove excess WGA. During the final wash, the cells were resuspended in 0.1 mg/mL PI solution.

Prior to imaging, the samples were loaded into an ibidi μ-Slide VI 0.4. Imaging was performed using a ZEISS Elyra 7 Super-Resolution Microscope equipped with a 63× Apochromat alpha Plan-Apochromat Oil immersion DIC objective, NA 1.4, and pco.edge sCMOS cameras. Lattice structured illumination images were acquired and processed using the ZEN black software at the Life Sciences and Engineering (LS&E) Infrastructure Center, Technion-Israel Institute of Technology, Haifa, Israel. The experiments were conducted three times with similar observations.

Thioflavin T fluorescence fibrillation kinetics assay

Thioflavin T (ThT) (Sigma Aldrich) is a widely used fluorescent dye for detecting and analyzing amyloid fibril formation kinetics. Fibrillation curves in the presence of ThT typically exhibit an initial lag phase followed by rapid fibril elongation. To accurately capture the fibrillation lag time, PSMα3 was pre-treated before the experiment. The peptide was dissolved in a 1:1 mixture of 1,1,1,3,3,3-Hexafluoroisopropanol (HFIP- Sigma Aldrich) and Trifluoroacetic acid (TFA- Sigma Aldrich) to a final concentration of 1 mg/mL, followed by bath sonication for 10 minutes at room temperature. The organic solvents were then evaporated using a mini-

rotational vacuum concentrator (Christ, Germany) at 1,000 rpm for 2 hours at room temperature.

For the experiment, freshly prepared 100 µM PSMα3 peptides, with or without 500 µM Epigallocatechin gallate (EGCG) at a 1:5 molar ratio, were prepared in 50 mM HEPES buffer pH 7.4 containing 150 mM NaCl. ThT was prepared by diluting a stock solution in ultrapure double-distilled water (UPddw) and filtered before use to reach a final concentration of 200 µM Blank control solutions containing all components except for the peptide were prepared for each reaction.

The assay was conducted in black 96-well flat-bottom plates (Greiner Bio-One), which were sealed with a thermal seal film (EXCEL Scientific) to prevent evaporation. Samples were incubated in a plate reader (OMEGA) at 37°C, shaking at 500 rpm for 85 seconds before each reading cycle, for up to 1,000 cycles of 6 minutes each, totaling approximately 100 hours. Fluorescence was measured in triplicate using an excitation wavelength of 438 ± 20 nm and an emission wavelength of 490 ± 20 nm. All values were averaged, background fluorescence was subtracted using blank controls, and the results were plotted over time. Standard error of the mean is shown as error bars. The entire experiment was independently repeated at least three times on different days to ensure reproducibility.

Solid-State Circular Dichroism Spectroscopy

Solid-state circular dichroism spectroscopy(ss-CD) was conducted with PSMa3 to assess their fibrillar secondary structure components in presence and absence of Poly (AU) RNA. For preparation of peptide and RNA samples, see Peptide and Poly (AU) preparation section. PSMa3 was prepared at a working concentration of 100 µM in 50 mM HEPES, pH 7.4, 150 mM NaCl at 0 ng/µL, 50 ng/µL or 400 ng/µL Poly (AU) RNA. The reaction mixes were incubated for 0 min, 2 h and 72 h at 37 °C in a non-shaking thermocycler. Following incubation, soluble reaction components were removed via dilution washing with 150 µL water and centrifugation at 12.500 rcf for 30 min. 20 µL of the sediment were resuspended in 180 µL water for a second washing centrifugation step at 12.500 rcf for 30 min. 180 µL of the

supernatant were discarded and 18 µL of sediment applied to a *Chirascan Series fused silica disc* (AP/CSSD, Applied Photophysics) in three times 6 µL steps. After every sample application onto to the silica disc, all liquid was evaporated at 37 °C for 5–10 min until only an opaque film remained visible. For secondary structure determination of aggregated/fibrillar peptide components on the silica disc, the disc was inserted into a *Chirascan solid sample holder* (CS/SSH, Applied Photophysics) and the circular dichroism recorded in the far-UV (180–250 nm, step size 1 nm, time-per-point 1 s) using a CD spectropolarimeter (Applied Photophysics). To counteract sample anisotropy, CD spectra were recorded at least four different disc rotations and the results averaged. Prior to data analysis, silica disc and buffer/water backgrounds were subtracted from recorded sample spectra. Poly (AU) RNA-only background spectra showed complex and high amplitude signals that did not appear for samples in combination with peptides and were therefore not subtracted from sample spectra.

NMR experiments

To prepare the reference samples for NMR analysis, 0.521 mg of PSMα3 was dissolved in 180 µL of 20 mM MES (2-(N-morpholino)ethanesulfonic acid) buffer at pH 6.0, supplemented with 5% (v/v) deuterium oxide (D_2O). From this solution, 170 µL was transferred into a 3.0 mm NMR tube for spectral acquisition. In parallel, a 4 mM stock solution of EGCG was prepared in the same 20 mM MES buffer (pH 6.0). From this, a working solution containing 0.5 mM EGCG in 20 mM MES with 5% (v/v) D_2O was prepared to match the buffer conditions of the peptide sample. A volume of 170 µL was then transferred into a separate 3.0 mm NMR tube for use as the EGCG reference.

All NMR experiments were recorded on a Bruker 700 MHz spectrometer equipped with a triple-resonance cryoprobe (Prodigy) and an AVANCE NEO console. One-dimensional (1D) ^{1}H-NMR spectra were acquired using the Bruker library pulse sequence zggpw5 for water suppression. The acquisition parameters were: acquisition time (AQ) = 1.90 s, spectral width (SW) = 12.31 ppm, recovery delay (D1) = 1.5 s, and 64 scans. All experiments were conducted at 35 °C, under which optimal spectral quality was obtained.

Two-dimensional (2D) ^{1}H–^{1}H TOCSY (Total Correlation Spectroscopy) spectra were collected using the Bruker pulse sequence dipsi2gpph19. Acquisition parameters were: t_2 = 2048 complex points (AQ_2 = 0.118 s), t_1 = 512 complex points (AQ_1 = 0.029 s), SW_1 = SW_2 = 12.31 ppm, with 64 scans and a mixing time (tmix) of 80 ms. Recovery delay (D1) was set to 1.5 s. 2D ^{1}H–^{1}H NOESY (Nuclear Overhauser Effect Spectroscopy) spectra were acquired using the noesyfpgpph19 pulse sequence, with acquisition parameters identical to those used for TOCSY. The mixing time was set to 300 ms. Total experimental time for the combined 2D TOCSY and NOESY experiments was approximately 30 hours. NMR data processing was carried out using TopSpin 4.5.0 (Bruker), and spectral assignments for the 2D TOCSY and NOESY spectra were performed using POKY software[68]. Signal integration was carried out using in-house scripts written in Scilab[69].

Acknowledgements

M.L. acknowledges research support from the Israel Science Foundation, Grant No. 2111/20 and the Cure Alzheimer's Fund. M.L. and M.Z. acknowledge the Forschungskooperation Niedersachsen – Israel, Volkswagenstiftung, No: 76251-4659/2022 (ZN 4042). Funded/Co-funded by the European Union (ERC, FuncAmyloid, 101087140). Views and opinions expressed are however those of the author(s) only and do not necessarily reflect those of the European Union or the European Research Council. Neither the European Union nor the granting authority can be held responsible for them. A.K.B thanks the Novo Nordisk Foundation (Grant number NNFSA17002839) and the European Union (ERC CoG 101088163 EMMA) for funding. We thank Ayala Shiber for advice and guidance, as well as Yael Mandel-Gutfreund and Hiba Hassanain for their assistance with RNA preparations. We acknowledge guidance and support from Nitsan Dahan from the Microscopy core facility center at the Lorry I. Lokey Interdisciplinary Center for Life Sciences and Engineering. We acknowledge the use of OpenAI's GPT-4 model to improve the writing quality of parts of this manuscript.

References

1. Zaman, M. & Andreasen, M. Cross-talk between individual phenol-soluble modulins in Staphylococcus aureus biofilm enables rapid and efficient amyloid formation. *eLife* **9**, e59776 (2020).
2. Barnhart, M. M. & Chapman, M. R. Curli biogenesis and function. *Annu Rev Microbiol* **60**, 131–147 (2006).
3. Rayan, B., Barnea, E., Khokhlov, A., Upcher, A. & Landau, M. Differential fibril morphologies and thermostability determine functional roles of Staphylococcus aureus PSMα1 and PSMα3. *Front Mol Biosci* **10**, 1184785 (2023).
4. Marinelli, P., Pallares, I., Navarro, S. & Ventura, S. Dissecting the contribution of Staphylococcus aureus α-phenol-soluble modulins to biofilm amyloid structure. *Sci Rep* **6**, 34552 (2016).
5. Schwartz, K., Syed, A. K., Stephenson, R. E., Rickard, A. H. & Boles, B. R. Functional amyloids composed of phenol soluble modulins stabilize Staphylococcus aureus biofilms. *PLoS Pathog* **8**, e1002744 (2012).
6. Sleutel, M., Pradhan, B., Volkov, A. N. & Remaut, H. Structural analysis and architectural principles of the bacterial amyloid curli. *Nat Commun* **14**, 2822 (2023).
7. Perov, S. *et al.* Structural Insights into Curli CsgA Cross-β Fibril Architecture Inspire Repurposing of Anti-amyloid Compounds as Anti-biofilm Agents. *PLoS Pathog* **15**, e1007978 (2019).
8. Howard, M. K. *et al.* Probing the drivers of Staphylococcus aureus biofilm protein amyloidogenesis and disrupting biofilms with engineered protein disaggregases. *mBio* **14**, e00587-23 (2023).
9. Chapman, M. R. *et al.* Role of Escherichia coli curli operons in directing amyloid fiber formation. *Science* **295**, 851–855 (2002).
10. Blanco, L. P., Evans, M. L., Smith, D. R., Badtke, M. P. & Chapman, M. R. Diversity, biogenesis and function of microbial amyloids. *Trends Microbiol* **20**, 66–73 (2012).
11. Le, K. Y., Dastgheyb, S., Ho, T. V. & Otto, M. Molecular determinants of staphylococcal biofilm dispersal and structuring. *Front Cell Infect Microbiol* **4**, 167 (2014).
12. Peschel, A. & Otto, M. Phenol-soluble modulins and staphylococcal infection. *Nat Rev Microbiol* **11**, 667–673 (2013).

13. Mehlin, C., Headley, C. M. & Klebanoff, S. J. An Inflammatory Polypeptide Complex from Staphylococcus epidermidis: Isolation and Characterization. *J Exp Med* **189**, 907–918 (1999).
14. Chatterjee, S. S. *et al.* Essential Staphylococcus aureus toxin export system. *Nat Med* **19**, 364–367 (2013).
15. Kretschmer, D. *et al.* Human formyl peptide receptor 2 senses highly pathogenic Staphylococcus aureus. *Cell Host Microbe* **7**, 463–473 (2010).
16. Queck, S. Y. *et al.* Mobile Genetic Element-Encoded Cytolysin Connects Virulence to Methicillin Resistance in MRSA. *PLoS Pathog* **5**, e1000533 (2009).
17. Joo, H.-S. & Otto, M. Molecular basis of in vivo biofilm formation by bacterial pathogens. *Chem Biol* **19**, 1503–1513 (2012).
18. Hu, Z. *et al.* Phenol-soluble modulin α and β display divergent roles in mice with staphylococcal septic arthritis. *Commun Biol* **5**, 1–11 (2022).
19. Grando, K. *et al.* Phenol-Soluble Modulins From Staphylococcus aureus Biofilms Form Complexes With DNA to Drive Autoimmunity. *Front Cell Infect Microbiol* **12**, 884065 (2022).
20. Cheung, G. Y. C., Joo, H.-S., Chatterjee, S. S. & Otto, M. Phenol-soluble modulins--critical determinants of staphylococcal virulence. *FEMS Microbiol Rev* **38**, 698–719 (2014).
21. Schwartz, K. *et al.* The AgrD N-terminal leader peptide of Staphylococcus aureus has cytolytic and amyloidogenic properties. *Infect Immun* **82**, 3837–3844 (2014).
22. Tayeb-Fligelman, E., Salinas, N., Tabachnikov, O. & Landau, M. Staphylococcus aureus PSMα3 Cross-α Fibril Polymorphism and Determinants of Cytotoxicity. *Structure* **28**, 301-313.e6 (2020).
23. Tayeb-Fligelman, E. *et al.* The cytotoxic Staphylococcus aureus PSMα3 reveals a cross-α amyloid-like fibril. *Science* **355**, 831–833 (2017).
24. Kreutzberger, M. A. B. *et al.* Phenol-soluble modulins PSMα3 and PSMβ2 form nanotubes that are cross-α amyloids. *Proc Natl Acad Sci U S A* **119**, e2121586119 (2022).
25. Schwartz, K. & Boles, B. R. Microbial amyloids--functions and interactions within the host. *Curr Opin Microbiol* **16**, 93–99 (2013).
26. Malishev, R. *et al.* Reciprocal Interactions between Membrane Bilayers and S. aureus PSMα3 Cross-α Amyloid Fibrils Account for Species-Specific Cytotoxicity. *J Mol Biol* **430**, 1431–1441 (2018).
27. Sancho-Vaello, E. *et al.* The structure of the antimicrobial human cathelicidin LL-37 shows oligomerization and channel formation in the presence of membrane mimics. *Sci Rep* **10**, 17356 (2020).
28. Engelberg, Y. & Landau, M. The Human LL-37(17-29) antimicrobial peptide reveals a functional supramolecular structure. *Nat Commun* **11**, 3894 (2020).
29. Rumpret, M. *et al.* Signal inhibitory receptor on leukocytes-1 recognizes bacterial and endogenous amphipathic α-helical peptides. *FASEB J* **35**, e21875 (2021).
30. Golan, N., Engelberg, Y. & Landau, M. Structural Mimicry in Microbial and Antimicrobial Amyloids. *Annual Review of Biochemistry* **91**, 403–422 (2022).
31. Rautenberg, M., Joo, H.-S., Otto, M. & Peschel, A. Neutrophil responses to staphylococcal pathogens and commensals via the formyl peptide receptor 2 relates to phenol-soluble modulin release and virulence. *FASEB J* **25**, 1254–1263 (2011).
32. Syed, A. K., Reed, T. J., Clark, K. L., Boles, B. R. & Kahlenberg, J. M. Staphlyococcus aureus phenol-soluble modulins stimulate the release of proinflammatory cytokines from keratinocytes and are required for induction of skin inflammation. *Infect Immun* **83**, 3428–3437 (2015).

33. Schreiner, J. *et al.* Staphylococcus aureus phenol-soluble modulin peptides modulate dendritic cell functions and increase in vitro priming of regulatory T cells. *J Immunol* **190**, 3417–3426 (2013).
34. Chu, M. *et al.* Staphylococcus aureus Phenol-Soluble Modulins α1-α3 Act as Novel Toll-Like Receptor (TLR) 4 Antagonists to Inhibit HMGB1/TLR4/NF-κB Signaling Pathway. *Front Immunol* **9**, 862 (2018).
35. Kretschmer, D., Nikola, N., Dürr, M., Otto, M. & Peschel, A. The Virulence Regulator Agr Controls the Staphylococcal Capacity to Activate Human Neutrophils via the Formyl Peptide Receptor 2. *J Innate Immun* **4**, 201–212 (2012).
36. Bröker, B. M., Mrochen, D. & Péton, V. The T Cell Response to Staphylococcus aureus. *Pathogens* **5**, 31 (2016).
37. Ganguly, D. *et al.* Self-RNA-antimicrobial peptide complexes activate human dendritic cells through TLR7 and TLR8. *J Exp Med* **206**, 1983–1994 (2009).
38. Tewary, P. *et al.* β-Defensin 2 and 3 promote the uptake of self or CpG DNA, enhance IFN-α production by human plasmacytoid dendritic cells, and promote inflammation. *J Immunol* **191**, 865–874 (2013).
39. Schmidt, N. W. *et al.* Liquid-crystalline ordering of antimicrobial peptide-DNA complexes controls TLR9 activation. *Nat Mater* **14**, 696–700 (2015).
40. Lee, E. Y. *et al.* Helical antimicrobial peptides assemble into protofibril scaffolds that present ordered dsDNA to TLR9. *Nat Commun* **10**, 1012 (2019).
41. Grando, K. *et al.* Phenol-Soluble Modulins From Staphylococcus aureus Biofilms Form Complexes With DNA to Drive Autoimmunity. *Front Cell Infect Microbiol* **12**, 884065 (2022).
42. Gallo, P. M. *et al.* Amyloid-DNA Composites of Bacterial Biofilms Stimulate Autoimmunity. *Immunity* **42**, 1171–1184 (2015).
43. Tursi, S. A. *et al.* Bacterial amyloid curli acts as a carrier for DNA to elicit an autoimmune response via TLR2 and TLR9. *PLOS Pathogens* **13**, e1006315 (2017).
44. Alberti, S., Gladfelter, A. & Mittag, T. Considerations and Challenges in Studying Liquid-Liquid Phase Separation and Biomolecular Condensates. *Cell* **176**, 419–434 (2019).
45. Aa, H., Ca, W. & F, J. Liquid-liquid phase separation in biology. *Annual review of cell and developmental biology* **30**, (2014).
46. B, W. *et al.* Liquid-liquid phase separation in human health and diseases. *Signal transduction and targeted therapy* **6**, (2021).
47. Xu, Z., Wang, W., Cao, Y. & Xue, B. Liquid-liquid phase separation: Fundamental physical principles, biological implications, and applications in supramolecular materials engineering. *Supramolecular Materials* **2**, 100049 (2023).
48. Indig, R. Y. & Landau, M. Designed inhibitors to reduce amyloid virulence and cytotoxicity and combat neurodegenerative and infectious diseases. *Current Opinion in Chemical Biology* **75**, 102318 (2023).
49. Fernandes, L., Cardim-Pires, T. R., Foguel, D. & Palhano, F. L. Green Tea Polyphenol Epigallocatechin-Gallate in Amyloid Aggregation and Neurodegenerative Diseases. *Front Neurosci* **15**, 718188 (2021).
50. Andrich, K. & Bieschke, J. The Effect of (-)-Epigallo-catechin-(3)-gallate on Amyloidogenic Proteins Suggests a Common Mechanism. *Adv Exp Med Biol* **863**, 139–161 (2015).
51. Nott, T. J. *et al.* Phase Transition of a Disordered Nuage Protein Generates Environmentally Responsive Membraneless Organelles. *Mol Cell* **57**, 936–947 (2015).

52. Sternke-Hoffmann, R., Peduzzo, A., Bolakhrif, N., Haas, R. & Buell, A. K. The Aggregation Conditions Define Whether EGCG is an Inhibitor or Enhancer of α-Synuclein Amyloid Fibril Formation. *Int J Mol Sci* **21**, 1995 (2020).
53. Riback, J. A. *et al.* Stress-Triggered Phase Separation Is an Adaptive, Evolutionarily Tuned Response. *Cell* **168**, 1028-1040.e19 (2017).
54. De Lorenzi, E. *et al.* Evidence that the Human Innate Immune Peptide LL-37 may be a Binding Partner of Amyloid-β and Inhibitor of Fibril Assembly. *J Alzheimers Dis* **59**, 1213–1226 (2017).
55. Murakami, T. *et al.* ALS/FTD Mutation-Induced Phase Transition of FUS Liquid Droplets and Reversible Hydrogels into Irreversible Hydrogels Impairs RNP Granule Function. *Neuron* **88**, 678–690 (2015).
56. Wang, Y.-L. *et al.* Liquid-liquid phase separation in DNA double-strand breaks repair. *Cell Death Dis* **14**, 1–10 (2023).
57. Kanaan, N. M., Hamel, C., Grabinski, T. & Combs, B. Liquid-liquid phase separation induces pathogenic tau conformations in vitro. *Nat Commun* **11**, 2809 (2020).
58. Ambadipudi, S., Biernat, J., Riedel, D., Mandelkow, E. & Zweckstetter, M. Liquid–liquid phase separation of the microtubule-binding repeats of the Alzheimer-related protein Tau. *Nat Commun* **8**, 275 (2017).
59. Boyko, S. & Surewicz, W. K. Tau liquid–liquid phase separation in neurodegenerative diseases. *Trends in Cell Biology* **32**, 611–623 (2022).
60. Wegmann, S. *et al.* Tau protein liquid–liquid phase separation can initiate tau aggregation. *The EMBO Journal* (2018) doi:10.15252/embj.201798049.
61. Babinchak, W. M. *et al.* The role of liquid–liquid phase separation in aggregation of the TDP-43 low-complexity domain. *Journal of Biological Chemistry* **294**, 6306–6317 (2019).
62. Mukherjee, S., Poudyal, M., Dave, K., Kadu, P. & Maji, S. K. Protein misfolding and amyloid nucleation through liquid–liquid phase separation. *Chem. Soc. Rev.* **53**, 4976–5013 (2024).
63. Ray, S. *et al.* α-Synuclein aggregation nucleates through liquid–liquid phase separation. *Nat. Chem.* **12**, 705–716 (2020).
64. Patel, A. *et al.* A Liquid-to-Solid Phase Transition of the ALS Protein FUS Accelerated by Disease Mutation. *Cell* **162**, 1066–1077 (2015).
65. Röntgen, A. *et al.* Aggregation of α-synuclein splice isoforms through a phase separation pathway. *Sci Adv* **11**, eadq5396 (2025).
66. Elbaum-Garfinkle, S. Matter over mind: Liquid phase separation and neurodegeneration. *J Biol Chem* **294**, 7160–7168 (2019).
67. Sneideris, T. *et al.* Targeting nucleic acid phase transitions as a mechanism of action for antimicrobial peptides. *Nat Commun* **14**, 7170 (2023).
68. Lee, W., Rahimi, M., Lee, Y. & Chiu, A. POKY: a software suite for multidimensional NMR and 3D structure calculation of biomolecules. *Bioinformatics* **37**, 3041–3042 (2021).
69. Campbell, S. L., Chancelier, J.-P. & Nikoukhah, R. Modeling and Simulation in Scilab. in *Modeling and Simulation in Scilab/Scicos with ScicosLab 4.4* 73–106 (Springer, New York, NY, 2010). doi:10.1007/978-1-4419-5527-2_3.

Supplementary Information

RNA Selectively Modulates Activity of Virulent Amyloid PSMα3 and Host Defense LL-37 via Phase Separation and Aggregation Dynamics

Rayan *et al.*

The supplementary information contains:

Figures S1-S9

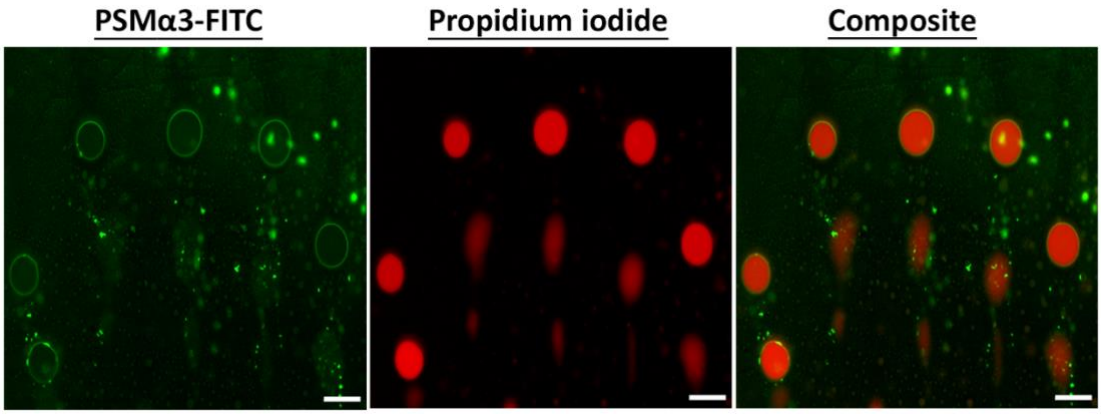

Figure S1. Encapsulation of Poly (AU) RNA within PSMα3-FITC droplets. FITC-PSMα3 (green) was mixed with 50 ng/μL Poly (AU) RNA labeled with PI. The left panel shows the FITC green channel, the middle panel displays the PI red channel, and the right panel is a composite image showing the overlap of PSMα3-FITC and Poly (AU) RNA-PI signals. Scale bars represent 20 μm.

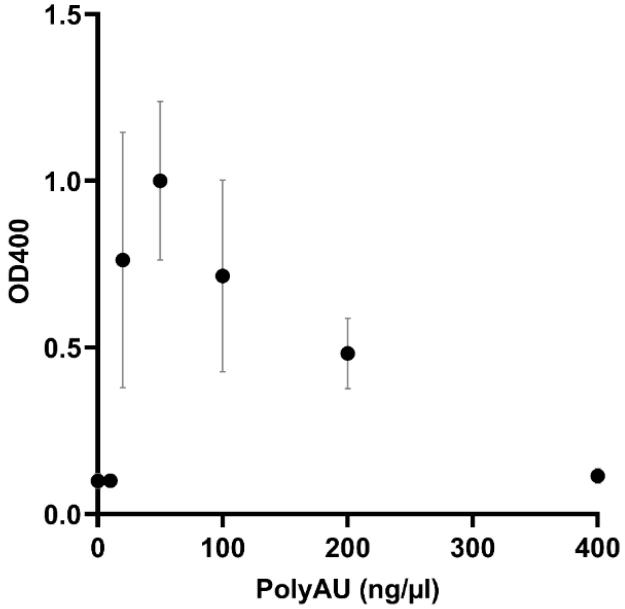

Figure S2. Turbidity measurements of PSMα3 with increasing Poly (AU) RNA concentrations. PSMα3 concentration was maintained at 100 μM, and Poly (AU) RNA concentrations varied across 0, 10, 20, 50, 100, 200, and 400 ng/μL. Data points represent the average optical density at 400 nm (OD400) recorded within the first 30 minutes post-resuspension, with each condition tested in triplicate. Error bars indicate the standard error of the mean.

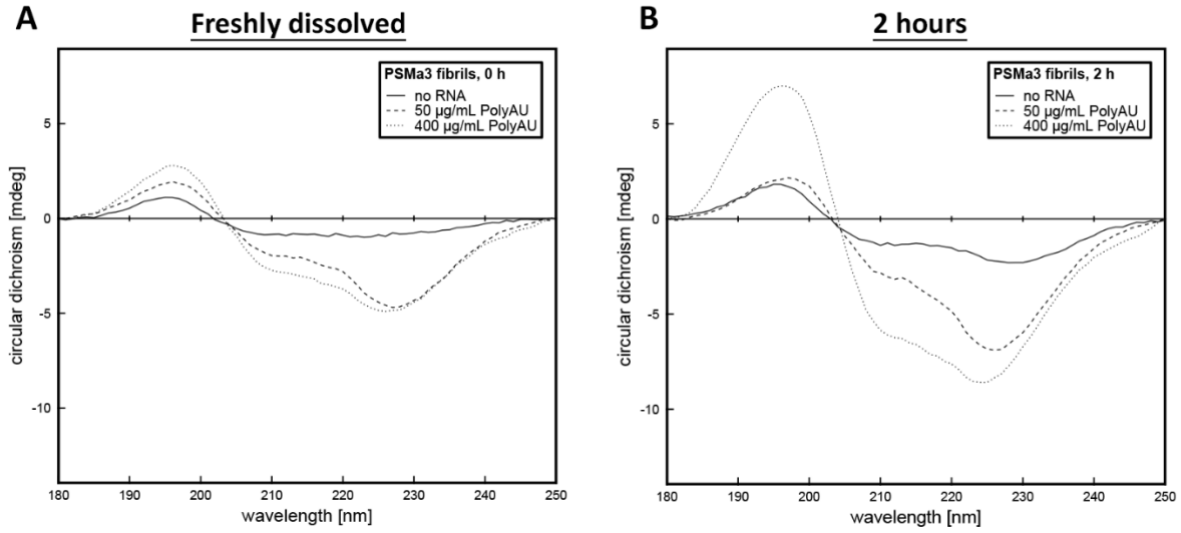

Figure S3. RNA stabilizes an α-helical conformation of PSMα3 over time. Solid-state circular dichroism (ssCD) spectra of PSMα3 incubated alone or with polyAU RNA at concentrations of 50 ng/µL and 400 ng/µL. Spectra were collected immediately after preparation (**A**), and after 2 hours of incubation (**B**). Measurements were recorded in the far-UV range (180–250 nm) to assess changes in secondary structure under the indicated conditions.

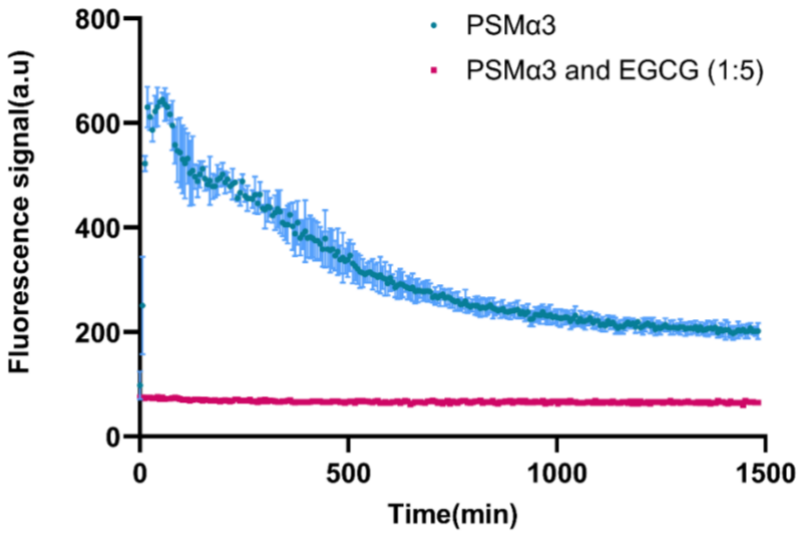

Figure S4. EGCG inhibits PSMα3 Fibrillation. Fibrillation kinetics of 100 µM freshly dissolved PSMα3, monitored by Thioflavin-T (ThT) fluorescence. The data compares PSMα3 fibrillation in the absence (blue curve) and presence (red curve) of EGCG. The graph displays the mean fluorescence intensities from triplicate ThT measurements, with error bars representing the standard error of the mean.

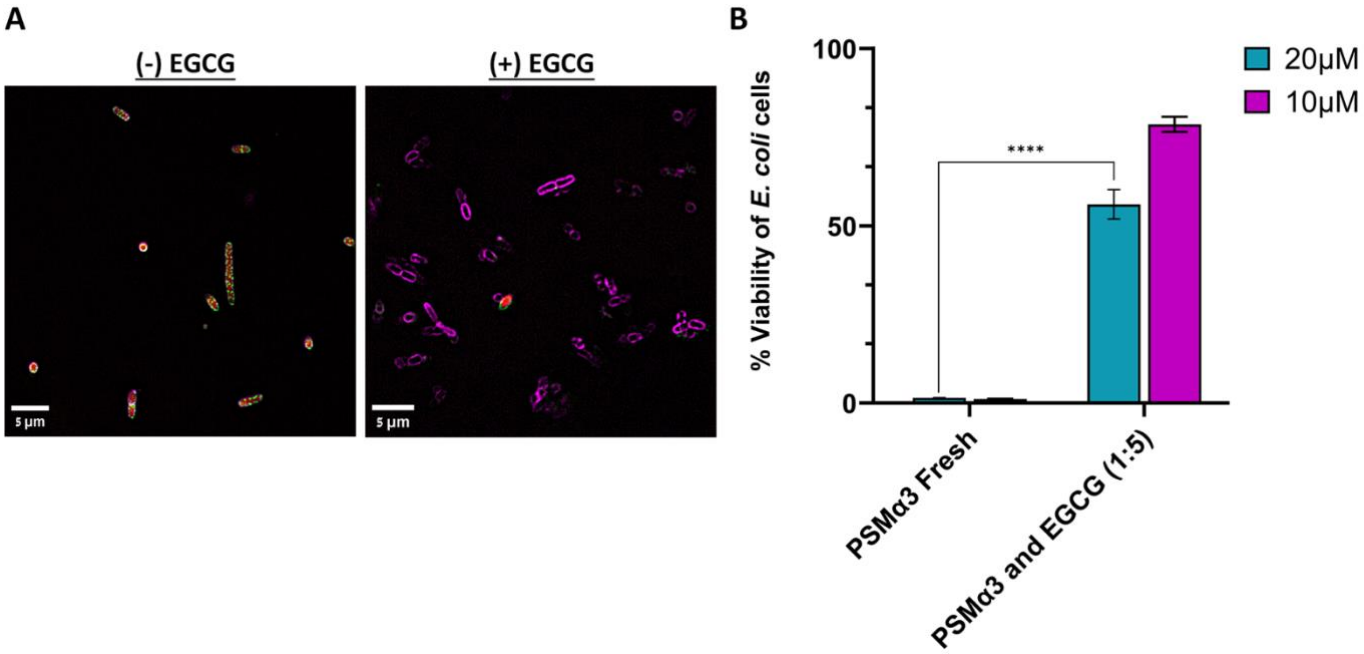

Figure S5. EGCG reduces the antimicrobial activity of PSMα3 against *E. coli*. (A) Super-resolution light microscopy images of E. coli treated with 20 µM PSMα3-FITC (green) in the absence (left) and presence (right) of EGCG at a 1:5 molar ratio. Scale bars: 5 µm. **(B)** Antimicrobial activity of PSMα3 against E. coli, evaluated using the PrestoBlue cell viability assay, with and without EGCG (1:5 molar ratio). The experiments were performed in at least three replicates and repeated across three independent days to ensure result reliability. Cytotoxicity and bacterial cell viability percentages were calculated as the mean of all replicates, with error bars representing the standard error of the mean (SEM). Statistical significance was determined using one-way ANOVA for normally distributed data in GraphPad Prism (version 11). Significance levels are indicated as follows: *$p<0.05$, **$p<0.01$, ***$p<0.001$, ****$p<0.0001$.

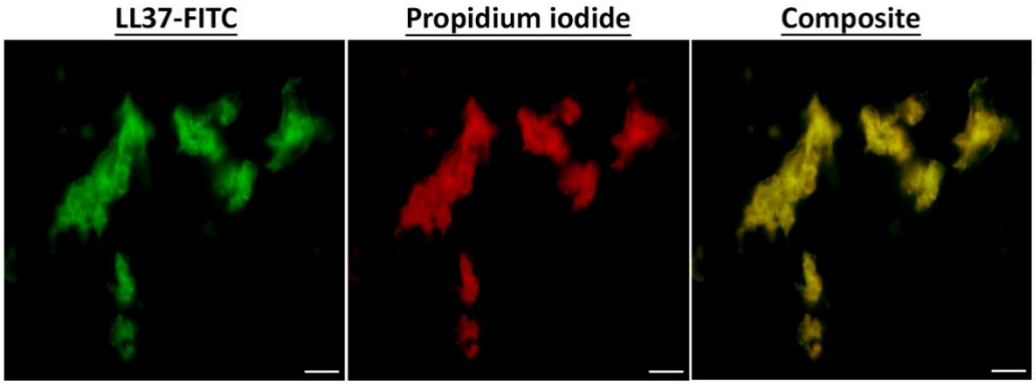

Figure S6. LL37 undergoes aggregation with Poly (AU) RNA before heat shock. Light microscopy images showing LL37-FITC (green) forming aggregates in the presence of 100 ng/μL Poly (AU) RNA, stained with propidium iodide (red). The composite image (right) highlights the colocalization of LL37 and RNA (yellow), indicating RNA-induced aggregation. Scale bars: 20 μm.

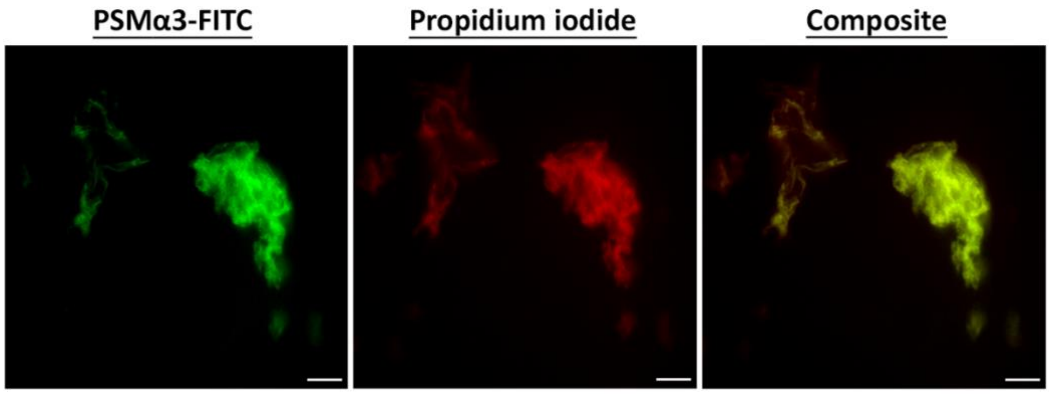

Figure S7. PSMα3 aggregates with Poly (AU) RNA after heat shock at physiological pH. Light microscopy images showing PSMα3-FITC (green) forming aggregates with 50 ng/μL Poly (AU) RNA, stained with propidium iodide (red), after heat shock at 60°C for 15 minutes in 50 mM HEPES, 150 mM NaCl, at physiological pH (7.4). The composite image (right) highlights the colocalization of PSMα3 and RNA (yellow), indicating RNA-induced aggregation under heat stress. Scale bars: 20 μm.

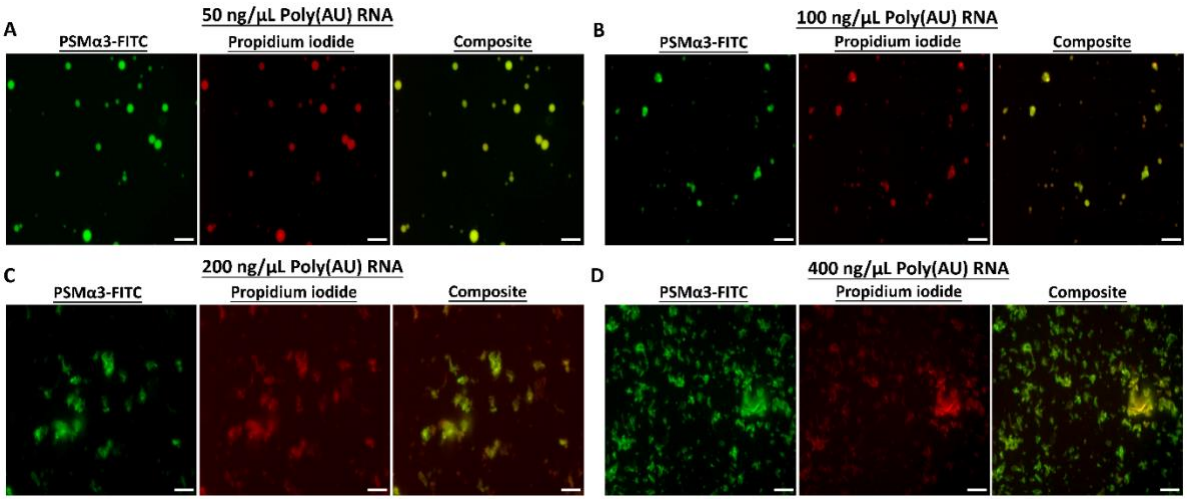

Figure S8. Effect of RNA concentration on PSMα3 phase separation and aggregation at pH 4 after heat shock. Fluorescence microscopy images showing the effects on PSMα3-FITC (green) in the presence of increasing concentrations of Poly (AU) RNA (labeled with Propidium Iodide, red) following heat shock at 65°C for 15 minutes at pH 4. at 50 ng/µL (**A**), 100 ng/µL (**B**), 200 ng/µL (**C**) and 400 ng/µL (**D**). At a low RNA concentration of 50 ng/µL (**A**), clear phase separation of PSMα3 was observed, as evidenced by the presence of well-defined, spherical droplets. As the RNA concentration increased to 100 ng/µL, the droplets began to lose their spherical structure and showed more morphological irregularities (**B**). At RNA concentrations of 200 ng/µL and 400 ng/µL, a distinct transition to aggregation with irregular, amorphous clusters were observed (**C** and **D**, respectively). The composite images revealed an overlap between the PSMα3 and RNA, indicating co-localization during both phase separation and amorphous cluster formation. Scale bars in all images represent 20 µm.

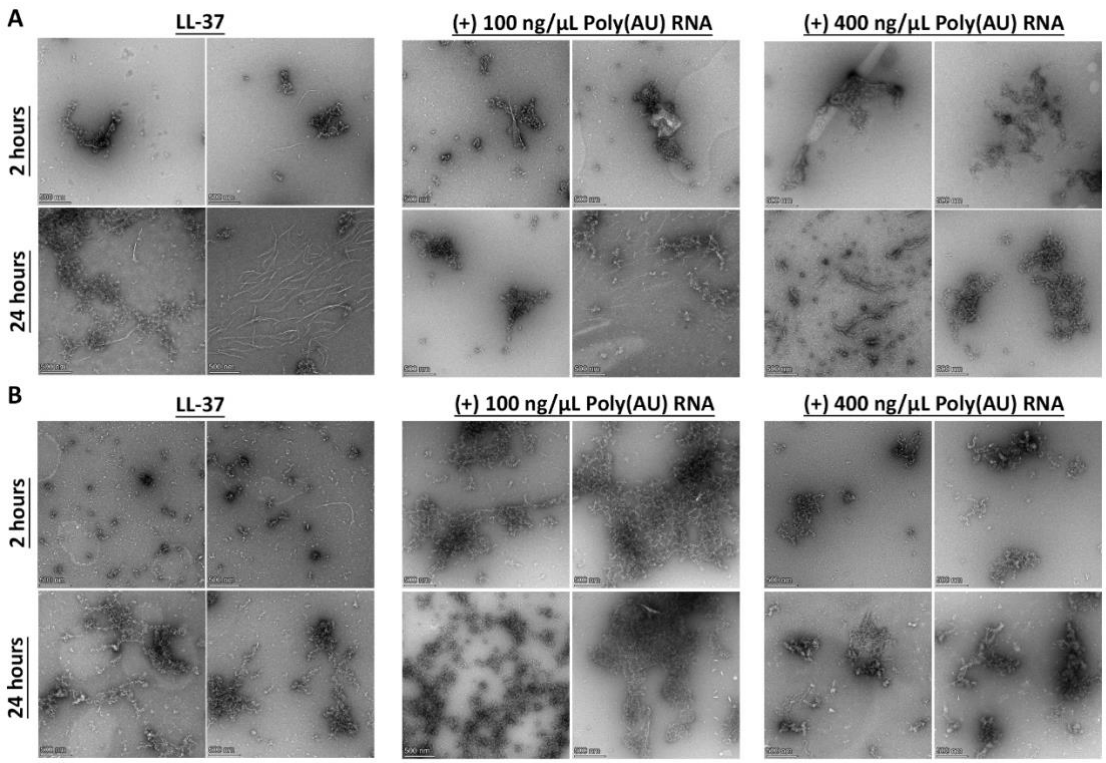

Figure S9. Poly (AU) RNA Modulates LL-37 Aggregation Dynamics Before and After Heat Shock. TEM micrographs of 100 µM LL-37 incubated alone or with 100 ng/µL or 400 ng/µL Poly (AU) RNA for 2 hours or 24 hours. **(A)** Samples imaged before heat shock at the indicated point. **(B)** Samples subjected to a 65°C heat shock for 15 minutes, followed by further incubation for 2 or 24 hours before imaging.